Seismology of adolescent neutron stars: Accounting for thermal effects and crust elasticity

C. J. Krüger, W. C. G. Ho, N. Andersson
Mathematical Sciences and STAG Research Centre,
University of Southampton, Southampton SO17 1BJ, United Kingdom

We study the oscillations of relativistic stars, incorporating key physics associated with internal composition, thermal gradients and crust elasticity. Our aim is to develop a formalism which is able to account for the state-of-the-art understanding of the complex physics associated with these systems. As a first step, we build models using a modern equation of state including composition gradients and density discontinuities associated with internal phase-transitions (like the crust-core transition and the point where muons first appear in the core). In order to understand the nature of the oscillation spectrum, we carry out cooling simulations to provide realistic snapshots of the temperature distribution in the interior as the star evolves through adolescence. The associated thermal pressure is incorporated in the perturbation analysis, and we discuss the presence of g-modes arising as a result of thermal effects. We also consider interface modes due to phase-transitions and the gradual formation of the star's crust, which leads to a set of shear modes.

arXiv:1402.5656v1 [gr-qc] 23 Feb 2014

I. INTRODUCTION

Neutron stars are seismically complex, with particular classes of oscillation modes associated with specific parts of the involved physics. This makes the construction of a truly realistic model of the star's oscillation spectrum a complicated task. Nevertheless, we are reaching the point where much of the physics involved is understood at the level required to build moderately realistic models. The aim of this work is thus quite natural; we want to take important steps towards realism by accounting for processes that are relevant as a neutron star matures. We achieve this by tracking the cooling of a given star from a minute or so after birth through the first several hundred years, paying particular attention to the changes in the thermal pressure and the formation of that star's elastic crust. The output from our state-of-the-art cooling code provides input for the seismology analysis. The results provide a sequence of snapshots of how the star's oscillation spectrum evolves as the star ages. This is an important advance on previous work in this area.

The problem of relativistic star seismology has been considered since pioneering work by Thorne & Campolattaro in the late 1960s [1]. Like much of the subsequent work, the initial focus was on the mathematical formulation of the problem with the complex supranuclear physics taking a secondary role. Thus, the bulk of the literature is focussed on perfect fluid stars, often without any consideration of the interior composition and state of matter. In fact, many studies have made use of rather ad hoc polytropic models which only capture the rough properties of a realistic equation of state. This has led to an understanding of the basic nature of the stellar spectrum, like the fundamental f-mode and the pressure restored p-modes [2, 3], and some discoveries, like the existence of the gravitational-wave w-modes, [4]. However, the understanding of the fine details of the problem has so far been developed one piece at a time. Gravity g-modes arising because of composition gradients have been considered [5–8], the crust elasticity has been accounted for (especially for shear modes) [9], the roles of core superfluidity [10–12] and the star's magnetic field [13–16] have been investigated and oscillations of proto-neutron stars and their detectability [17] have been studied, as well. In the last decade, much attention has been focussed on the Coriolis restored r-modes [18–21], which are relevant because they may be driven unstable due to the gravitational radiation they generate. In this context, much of the complex microphysics related to dissipative processes has been discussed, progressing our understanding of the involved processes considerably.

Neutron star oscillations may impact on a range of observations, involving in particular radio and X-ray timing and gravitational waves. At the present time, the most promising connection between observations and theory is provided by the observed quasiperiodic oscillations seen in the X-ray tail of magnetar giant flares [22, 23]. The inferred oscillation frequencies match those expected from the elastic crust reasonably well, and provide the first credible example of actual neutron star asteroseismology. There are, of course, issues to be resolved especially concerning the dynamical role of the interior magnetic field in these systems [24]. A more indirect example comes from X-ray timing of fast spinning accreting neutron stars in Low-Mass X-ray Binaries [25, 26]. The spin of these stars appears to be limited by some process. One of the leading contenders for the underlying mechanism is the r-mode instability which leads to the star losing angular momentum at a rate that could balance the spin-up due to accretion [27, 28]. Finally, as we are getting closer to the advent of gravitational-wave astronomy, there has been searches for neutron star oscillations from a range of systems [29–32]. At present, these studies may only be providing relatively uninteresting upper limits on the possible signals. With an advanced generation of detectors coming online in the next few years,

this could turn to actual detections.

The existing body of work allows us to piece together a picture of neutron star dynamics. This understanding should be valid provided the star is in a regime where the different ingredients remain distinct. Unfortunately, this is unlikely to be the case. Hence, there is a pressing need to develop a new generation of models that account for as much of the relevant physics as possible. The present work should be seen in that context.

The physics associated with realistic neutron star dynamics is daunting. Many aspects are rather poorly understood, in particular concerning the deep core (at several times the nuclear saturation density). Nevertheless, a focussed effort on this problem is timely. First of all, gravitational-wave astronomy should become reality in the next few years. This promises to provide us with observational data (perhaps most likely from the merger of compact binaries) that need to be matched against the best possible theoretical models. Secondly, our understanding of the principles associated with neutron star superfluidity has improved considerably in the last decade. In particular, we have real constraints on the superfluid parameters from the observed real-time cooling of the remnant in Cassiopeia A [33]. This constrains the superfluid pairing gaps (or equivalently, the critical temperatures). In order to be able to make productive use of future observational results, we need to improve our level of modelling.

The basic requirement for progress on this problem is a realistic equation of state which accounts for the two-fluid nature of a neutron star's core, including information about the superfluid gap energies and the entrainment parameters. We also need a comprehensive formalism for modelling dynamics which accounts for all the desired parameters. Progress on the first of these issues was recently made by Chamel [34], who provided the first ever consistent equation of state including entrainment. The second problem has been explored in basic models [35], basically to the point where there are no technical stumbling blocks preventing more realistic studies.

In this work we take the first steps towards true realism, starting from the classic fluid formalism of Detweiler & Lindblom [3] and extending it to account for density discontinuities associated with distinct phase-transitions, interior composition gradients, thermal pressure, and the elastic crust which will form and grow in thickness as the neutron star cools. We use this model to study the evolution of the star's oscillation modes as it matures. To do this we couple the oscillation mode calculation to the long-term cooling of the star. At different points in the thermal evolution we output the temperature profile and feed it into the mode calculation. The results of this exercise shed light on the influence of thermal effects on the various oscillation modes of the star. As expected, we find that the fundamental f-mode and the various p-modes are only weakly affected by the changes in temperature. Meanwhile, the gravity g-mode spectrum changes completely as the thermal pressure weakens and we demonstrate how only a few interface modes (arising from density "discontinuities") remain (in the considered frequency range above 10 Hz or so) when the star reaches maturity. Finally, the presence of the elastic crust enriches the spectrum by shear modes, which also evolve as the star cools and the crust region grows.

This paper is the first in a series where we aim to build a truly realistic model of a dynamical neutron star. Our initial focus is on issues relating to composition and thermal effects. This will lead naturally on to the role of superfluidity, which will be considered in a follow-up paper. The basic reason for the division is that the problems we consider here can be modelled within the standard single-fluid framework, while superfluidity adds degrees of freedom that make the problem richer (and obviously more complicated). The same is true for the star's magnetic field, which would eventually have to be included in the model (involving issues associated with the presence of a superconducting core [36]).

The layout of the paper is as follows: Section II is devoted to the physics which we take into account for the background model; in Section II E, we discuss the perturbation equations and explain how these are modified to account for additional physics (the perturbation equations for the elastic crust are given in Appendix A). A general numerical strategy for solving the perturbation equations in the interior of a multi-layered star is presented in Section III and Appendix C; Section III also covers the reasoning for a new set of equations for perturbations of the perfect fluid, which aids in solving the perturbation problem at low frequencies; the actual equations can be found in Appendix B. Finally, Section IV contains the results and Section V summarises our work. Unless stated otherwise, we use units in which $G = c = 1$ and Misner, Thorne and Wheeler (MTW) [37] conventions throughout the paper.

II. KEY ASPECTS OF THE MODEL

We aim to build a state-of-the-art neutron star model and track changes in its dynamics, represented by non-radial modes of oscillation, as the star evolves from just after birth into adolescence. The problem involves a number of unknowns, ranging from the bulk equation of state (e.g. pressure versus density in the deep core) to details of the microphysics (like the reactions that dictate the thermal evolution). In order to make progress, and avoid unnecessary confusion, it is necessary to make choices from the very beginning.

Given the uncertainties involved, much work on neutron-star seismology has considered a range of equations of state, aiming to establish to what extent observations can be used to distinguish between different models [38].

This is a useful strategy as it provides a foundation for future efforts to carry out the asteroseismology programme. However, it is not a practical approach for our present purposes. The many different options involved would cause undue confusion. Instead, we will assume that the physics input is known (even though it clearly is not!) at the required level of precision. This allows us to construct a unique sequence of stellar models. In order to be considered "realistic", this sequence must satisfy all current constraints from observations. In particular, the model must allow the maximum mass to be above $2M_\odot$ [39, 40] while the radius of a typical stellar model should lie in the range inferred from X-ray burst sources [41], i.e. $11.5 \pm 1.2\,\mathrm{km}$. Fortunately, the SLy4 equation of state [34, 42] satisfies these criteria. This model also suits our purposes by involving the simplest reasonable composition. The star's core contains only neutrons, protons, electrons and muons; there are no "exotic" components like hyperons or deconfined quarks.

Having fixed the equation of state, we still need to narrow the focus. We will consider a sample neutron star. The aim is to track the changes in the oscillation spectrum as this star ages. The particular star we consider has central density $\rho_c = 1 \times 10^{15}\,\mathrm{g\,cm^{-3}}$, which leads to a radius of $R = 11.77\,\mathrm{km}$ and a mass of $M = 1.45\,M_\odot$. This model star cools mainly due to modified Urca processes [43].

A. The Background Configuration

In order to solve the seismology problem, we first of all need a background solution. The construction of such a configuration is standard. The equilibrium of a non-rotating star with an unstrained crust is described by a static, spherically symmetric spacetime with metric g_{ab} of form

$$ds^2 = -e^\nu dt^2 + e^\lambda dr^2 + r^2 d\theta^2 + r^2 \sin^2\theta d\phi^2 \tag{1}$$

and the standard perfect fluid energy-momentum tensor

$$T_{ab} = (\rho + p) u_a u_b + p g_{ab}, \tag{2}$$

where ρ is the energy density and p the pressure. The fluid four-velocity is given by

$$u^a = e^{-\nu/2} t^a, \tag{3}$$

with $t^a = (\partial_t)^a$ the timelike Killing vector of the spacetime.

At finite temperatures, the pressure p is given by a two-parameter equation of state [72] (EoS henceforth) which depends on the energy density ρ and the temperature T (or the entropy density s). In the first few minutes after the star's birth, the thermal pressure is considerable and the star is puffed up to roughly twice its final radius. In order to simplify the analysis, we will not consider this stage. A study that complements ours in this respect has already been carried out [44]. In the following we consider models that are sufficiently cold that we can neglect the thermal pressure for the background configuration (but not for the perturbations!). In effect, this means that the star has to be colder than 10^{10} K or so. The background EoS can then be given in one-parameter form

$$p = p(\rho). \tag{4}$$

The Einstein equations lead to the well-known Tolman-Oppenheimer-Volkoff (TOV) equations

$$\lambda' = \frac{1 - e^\lambda}{r} + 8\pi r e^\lambda \rho, \tag{5}$$

$$\nu' = \frac{e^\lambda - 1}{r} + 8\pi r e^\lambda p, \tag{6}$$

$$p' = -\frac{1}{2}(\rho + p)\nu', \tag{7}$$

where a prime denotes a derivative with respect to r. We also define the mass inside radius r to be

$$M(r) = \frac{1}{2} r \left(1 - e^{-\lambda}\right). \tag{8}$$

Finally, the adiabatic index of the background configuration, which is assumed to be in β-equilibrium, is

$$\gamma_0 = \frac{\rho + p}{p} \frac{dp}{d\rho}. \tag{9}$$

B. The Equation of State

To model the star's core, we use the numerical fit to the SLy4 equation of state proposed by Chamel [34, 42]. This is a zero temperature EoS which accounts for the presence of a mixture of superfluid neutrons and superconducting protons in the core, and includes the entrainment effect. Estimates of the associated parameters are key to future developments of our model so it is natural to focus on this particular EoS already at this stage.

As a neutron star matures, the state of matter changes. The outer layers freeze to form the elastic crust and the core becomes a superfluid/superconducting mixture. We will account for the former, but postpone consideration of the latter. However, provided that the elastic crust has time to relax we do not have to account for the presence of strains in the background model. This effectively means that we are still dealing with pressure only as a function of the density. Our model makes use of the (simplified) EoS proposed by Douchin & Haensel (DH) [45], throughout the envelope and the crust, up to the pressure $p_m = 3.755 \times 10^{32}\,\mathrm{dyn\,cm^{-2}}$.

The matching of the two chosen EoS at the pressure p_m results in a small, artificial density discontinuity of $\Delta\rho/\rho_+ \approx 3.0\,\%$ at the crust-core transition (where ρ_+ is the density of the crustal matter at the transition). This piecing together of different EoSs might seem a bit ad-hoc; however, our main interest is in the development of the technology required to solve the problem. We aim to provide a proof of principle, not a truly accurate spectrum of a real neutron star. Of course, the computational technology is such that, if we are provided with the true EoS the analysis could proceed more or less in a plug-and-play fashion. Density discontinuities, such as the artificial one mentioned here are not a numerical problem but an expected feature. Within the crust of a neutron star where matter is formed from ions, there are several first order phase-transitions which come with a sudden change in density. The DH EoS accounts for 12 such phase-transitions and the associated density discontinuities are of similar size as our artificial one: $\Delta\rho/\rho_+$ varies between $2.0 - 4.3\,\%$ (where ρ_+ denotes the lower density of a discontinuity).

C. Thermal Evolution

In order to quantify the thermal effects on the star's oscillation spectrum, we carry out cooling simulations from $T \approx 10^{10}\,\mathrm{K}$, at which point the thermal pressure can be neglected compared to the static pressure. Starting from a uniform initial temperature profile (this is artificial but filters out of the system very rapidly), we evolve the interior temperature $T(r,t)$ of the neutron star using the relativistic equations of energy balance and heat flux [43]

$$\frac{e^{-\lambda/2-\nu}}{4\pi r^2}\frac{\partial}{\partial r}\left(e^{\nu}L_r\right) = -e^{-\nu/2}C\frac{\partial T}{\partial t} - \varepsilon_\nu, \tag{10}$$

$$\frac{L_r}{4\pi r^2} = -e^{-(\lambda+\nu)/2}K\frac{\partial}{\partial r}\left(e^{\nu/2}T\right), \tag{11}$$

where L_r is the luminosity at radius r, C is the heat capacity, ϵ_ν is the neutrino emissivity and K is the thermal conductivity. Note that we do not include internal heat sources, which would appear as a further source term in Equation (10); without these, neutron stars become essentially isothermal after about 100 years, as is apparent in Figure 1 where we show the thermal evolution of our chosen neutron star.

In order to provide a picture of what is involved, let us list the ingredients going into this calculation (for a detailed discussion we refer the reader to Ho et al. [43]). The total heat capacity C is the sum of the partial heat capacities. In the core, these are due to neutrons, protons, electrons and muons whereas in the crust there are contributions from free neutrons, ions and electrons [43, 46].

The neutrino emissivity ϵ_ν has several contributors as well and must be treated differently in the core and in the crust. In the core, we account for two classes of neutrino emission processes. First, we have the so-called modified Urca processes; we consider both the neutron and the proton branch. The direct Urca process, however, does not contribute since it occurs only at densities higher than those reached by the stellar model we consider here, for which the central density is $\rho_c = 1 \times 10^{15}\,\mathrm{g\,cm^{-3}}$. Second, we consider bremsstrahlung in which neutrino-antineutrino pairs are produced. In particular, we use emissivities due to neutron-neutron, neutron-proton and proton-proton scattering. The emissivities we use were calculated by Yakovlev et al. [47] and Page et al. [48]. In the crust, bremsstrahlung is still an important process and we consider electron-nucleon, neutron-neutron and neutron-nucleon scattering. Additionally, we consider the two processes of plasmon decay and electron-positron pair annihilation which both could in principle occur in the core but are much more efficient in low density regions like the crust. We take the emissivities for these processes from Yakovlev et al. [49, 50]. For the thermal conductivity of the core, we sum the contributions due to neutrons, electrons and muons [51, 52]. We take the results of Baiko et al. [53] for the neutron thermal conductivity and the results of Shternin & Yakovlev [54] for the electron and muon thermal conductivities. For the crust, we use CONDUCT08 [55], which implements the latest advances in calculating thermal conductivities [56–58].

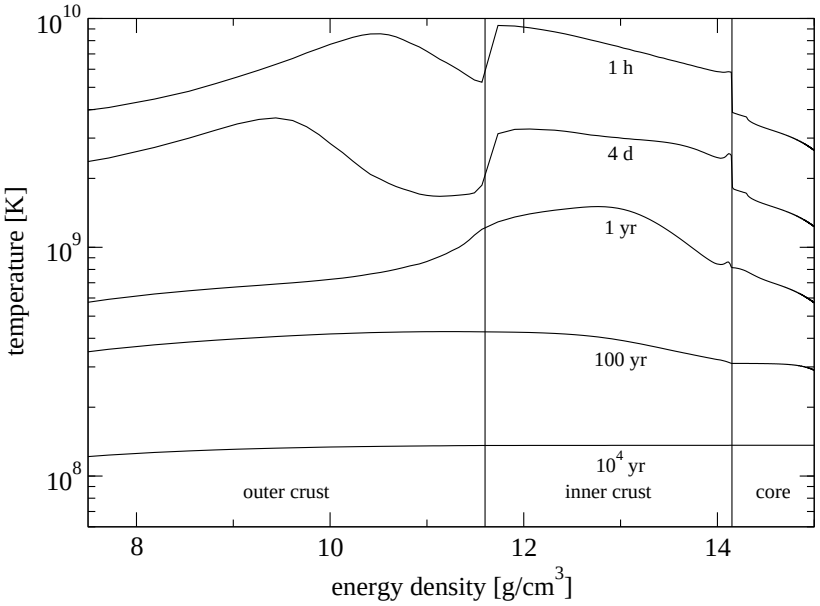

FIG. 1: The thermal evolution of our neutron star model with $M = 1.45\,M_\odot$. As is apparent from this graph, the neutron star is nearly isothermal after 100 years (without heat sources).

The outer layers — the envelope — of the crust serve as a heat blanket and can support large temperature gradients near the surface of the star [59]. The relationship between the temperature at the bottom of the envelope $T_{\rm env}$ and the effective temperature of the photosphere T_s depends on the composition of the envelope. We consider envelopes consisting of either iron or light elements and use relations between $T_{\rm env}$ and T_s given by Potekhin et al. [60].

As is apparent from Figure 1, the core of the neutron star cools more quickly than the crust in the very early stages of its life. This is due to stronger neutrino emission in the core and hence the crust is generally hotter than the core. In these very early stages, thermal conductivity does not play a major role in the cooling evolution and the cooling of the core and the crust can be considered more or less decoupled; this leads to the rather big jumps in temperature at the crust-core transition, see Figure 1. The jump between the outer and inner crust is due to the neutron drip. After about one year or so, the star has cooled considerably, so that the cooling mechanisms become less efficient and conductivity will smooth the temperature profile throughout the star, finally bringing it into an isothermal state after about 100 years.

D. Crust Formation

As one of our aims is to study shear modes associated with the crust elasticity, we have to specify the region in which the crust may sustain shear stress. That is, we need to quantify the solid region. The standard idealised model for the crust of a neutron star is a one-component plasma, in which ions of charge Ze, number density n and temperature T are free to move. The thermodynamics of such a plasma can be described by the dimensionless Coulomb coupling parameter

$$\Gamma = \frac{(Ze)^2}{akT}, \tag{12}$$

where $a = (4\pi n/3)^{-1/3}$ denotes the inter-ion spacing and k is the Boltzmann constant. Calculations by Farouki & Hamaguchi [61] show that the crust crystallises as Γ increases (due to cooling) above $\Gamma_m \approx 173$. The DH crust EoS (see Section II B) we are using provides us with all parameters required to quantify the crust freezing. Given the temperature profiles from our thermal evolution we calculate Γ and assume the crust to be elastic in the region in which $\Gamma \geq \Gamma_m$. The quantity Γ_m is associated with uncertainties of a few percent; a slightly different value will affect the thickness of the crust and thereby the frequencies of the shear modes. Similar to the choice of the EoS, we do not further investigate these effects in this study and take the value of $\Gamma_m = 173$ as given. It can easily be adjusted once more accurate data are available. In Figure 2, we show how the crust region evolves as the star cools.

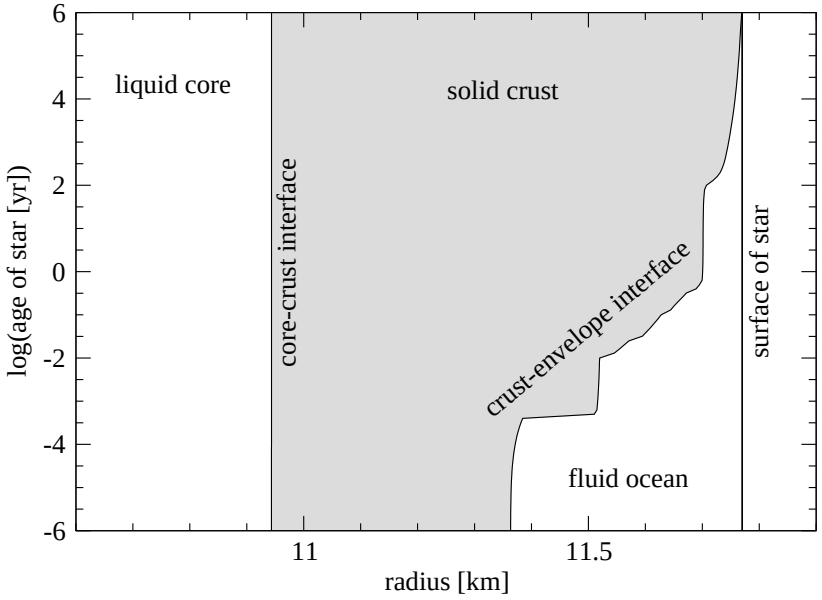

FIG. 2: The formation of the solid crust over time. We show only the outer layer of our model star. The area where the crust is crystallised is shaded in grey; this region is calculated using a sharp threshold of $\Gamma > 173$ (see text).

E. Perturbations

Our model accounts for several "restoring forces" expected to be present in a real neutron star, each of which results in a certain, more or less distinct class of modes in the stellar spectrum. The model considered here obviously has the standard f-mode (due to the presence of the star's surface) and acoustic p-modes, restored by the pressure. In addition we have composition gradients (leading to composition g-modes), a finite temperature (thermal g-modes), an elastic crust (s-modes) and density discontinuities (i-modes). In this section we discuss how the relevant physics enters the perturbation equations.

Before we describe the additional physics, we briefly mention basic definitions. We define the Lagragian displacement vector ξ^a to be

$$\xi^t = 0, \tag{13}$$

$$\xi^r = r^l e^{-\lambda/2} \frac{W}{r} P_l e^{i\omega t}, \tag{14}$$

$$\xi^\theta = -r^l \frac{V}{r^2} \frac{dP_l}{d\theta} e^{i\omega t}, \tag{15}$$

$$\xi^\phi = 0, \tag{16}$$

where W and V are functions of r and P_l are the Legendre polynomials. The velocity perturbation is then given by

$$\delta u^a = q^a_b \left(u^c \nabla_c \xi^b - \xi^c \nabla_c u^b \right) + \frac{1}{2} u^a u^b u^c h_{bc}, \tag{17}$$

with the projection tensor $q^{ab} = g^{ab} + u^a u^b$ and h_{ab} being the perturbed metric as given later (see Equation (27)).

Let us first consider the effects of internal stratification on a given perturbed fluid element. As the fluid moves, weak interaction processes try to adjust the composition to the surrounding matter and restore β-equilibrium. However, as Reisenegger & Goldreich [62] have argued, the timescale of the relevant weak interaction processes is much longer than the typical oscillation period and thus perturbed fluid elements are not able to equilibrate during one oscillation. In fact, it is usually appropriate to assume that the composition of a perturbed fluid element is frozen. This means that the adiabatic index γ of the perturbed fluid is

$$\gamma = \frac{\rho + p}{p} \left(\frac{\partial p}{\partial \rho} \right)_{n,T}, \tag{18}$$

where we assumed that the temperature T of the fluid element under consideration does not change either. We will refer to this as the *slow reaction* limit.

In order to understand the different classes of g-modes, it is useful to introduce the Schwarzschild discriminant

$$S = \frac{dp}{dr} - \frac{\gamma p}{\rho + p}\frac{d\rho}{dr} = \left(1 - \frac{\gamma}{\gamma_0}\right)\frac{dp}{dr}, \tag{19}$$

which determines the stability of a pulsating star against convection [63]. Stability requires that $S \geq 0$ throughout the star. For our particular equation of state this condition holds as we have $\gamma \geq \gamma_0$ everywhere. Note that we have used Equation (9) in order to achieve the last equality in Equation (19). Composition g-modes arise as the buoyancy associated with S provides a restoring force for small fluid-element deviations from equilibrium.

It may, of course, be the case that the dynamics is much slower than the weak interactions. In the limit of *fast reactions* the interactions are sufficiently fast to fully adjust the perturbed fluid element's composition such that it stays in β-equilibrium at all times. Such a star is called barotropic and the adiabatic indices, γ and γ_0, then coincide. As a consequence, the Schwarzschild discriminant vanishes, $S = 0$. In this case, perturbed fluid elements are not affected by buoyancy and the g-modes due to stratification are absent from the stellar spectrum.

Acting in a fashion similar to that of composition variations, the presence of a finite temperature in the star leads to a thermal pressure. Since our equation of state models zero temperature physics, we will account for thermal effects by adding a thermal pressure of form [64]

$$p_{th}^{\mathrm{x}}(n_{\mathrm{x}}, T) = \frac{\pi^2}{6} n_{\mathrm{x}} kT \frac{kT}{E_F^{\mathrm{x}}} \tag{20}$$

to the pressure at zero temperature. Here, n_{x} is the number density of the relevant species, x=n, p, e and μ for neutrons, protons, electrons and muons, respectively, k is the Boltzmann constant and E_F^{x} is the Fermi energy of the given species. As the electrons are relativistic, their Fermi energy is much higher than that of protons or neutrons and as a result their contribution to the thermal pressure is much lower in comparison. Hence, we will only account for thermal pressure due to neutrons and protons. The non-relativistic nucleon Fermi energy is given by $E_F^{\mathrm{x}} = p_{F\mathrm{x}}^2/2m$ with $p_{F\mathrm{x}} = \hbar k_F^{\mathrm{x}}$ and $k_F^{\mathrm{x}} = \left(3\pi^2 n_{\mathrm{x}}\right)^{1/3}$. Since the EoS gives us information about the composition of the neutron star core, we have all the information we need to account for the thermal pressure due to neutrons and protons, and the total pressure p becomes

$$p = p_0(\rho, x_{\mathrm{p}}) + \sum_{\mathrm{x=n,p}} p_{th}^{\mathrm{x}}(n_{\mathrm{x}}, T), \tag{21}$$

where p_0 is the pressure of the zero temperature equation of state described in Section II B and $x_{\mathrm{p}} = n_{\mathrm{p}}/n_b$ is the proton fraction ($n_b = n_{\mathrm{n}} + n_{\mathrm{p}}$ is the baryon number density). In order to see how the thermal pressure enters the perturbation equations, we have to calculate the perturbed pressure. Since we are assuming the composition to be frozen we have $\Delta x_{\mathrm{p}} = 0$, where Δ represents a Lagrangian perturbation. Meanwhile, adiabaticity implies $\Delta T = 0$, and hence we get for the perturbed pressure

$$\Delta p = \left(\frac{\partial p_0}{\partial \rho}\right)_{x_{\mathrm{p}}} \Delta\rho + \left(\frac{\partial p_{th}^{\mathrm{n}}}{\partial n_{\mathrm{n}}}\right)_T \Delta n_{\mathrm{n}} + \left(\frac{\partial p_{th}^{\mathrm{p}}}{\partial n_{\mathrm{p}}}\right)_T \Delta n_{\mathrm{p}} \tag{22}$$

Keeping in mind that the composition is frozen and therefore protons and neutrons are conserved separately, it follows [11] that

$$\frac{\Delta n_{\mathrm{n}}}{n_{\mathrm{n}}} = \frac{\Delta n_{\mathrm{p}}}{n_{\mathrm{p}}} = \frac{\Delta n_b}{n_b} \tag{23}$$

since both species are comoving, too. Using these relations we can eliminate Δn_{n} and Δn_{p} in favour of Δn_b and arrive at

$$\Delta p = \left[\gamma p_0 + n_{\mathrm{n}}\left(\frac{\partial p_{th}^{\mathrm{n}}}{\partial n_{\mathrm{n}}}\right)_T + n_{\mathrm{p}}\left(\frac{\partial p_{th}^{\mathrm{p}}}{\partial n_{\mathrm{p}}}\right)_T\right]\frac{\Delta n_b}{n_b}. \tag{24}$$

where we have made use of the thermodynamical relation (for $\Delta T = 0$)

$$\Delta\rho = \frac{\rho + p}{n_b}\Delta n_b \tag{25}$$

and the definition of γ (see Equation (18)). This provides us with a straightforward way to incorporate the thermal pressure in the perturbation problem.

It is not quite as straightforward to account for the elasticity of the star's crust, at least not in general. The approximation that the star is a perfect fluid has to be abandoned as soon as the solid crust forms, i.e. in the very early stages of a neutron star's life. The elastic crust supports shear stresses which by definition do not exist in a perfect fluid. To account for such stresses, we have to introduce off-diagonal terms in the stress-energy tensor. However, as we are assuming the background to be in a relaxed, unstrained state, these alterations only appear in the perturbed stress-energy tensor.

Following [65], the shear strain tensor is given by

$$\delta s^b_a = \frac{1}{2}\left(\perp^c_a \perp^{db} - \frac{1}{3}\perp^b_a \perp^{cd}\right)\Delta g_{cd}. \tag{26}$$

We will express the metric perturbations in the well-known Regge-Wheeler gauge [66]. This means that the components of the Eulerian perturbations of metric take the form

$$\delta g_{ab} = h_{ab} = -\begin{pmatrix} e^\nu r^l H_0(r) & r^{l+1}\dot{H}_1(r) & 0 & 0 \\ r^{l+1}\dot{H}_1(r) & e^\lambda r^l H_2(r) & 0 & 0 \\ 0 & 0 & r^{l+2}K(r) & 0 \\ 0 & 0 & 0 & r^{l+2}\sin^2\theta K(r) \end{pmatrix} P_l(\cos\theta)e^{i\omega t}, \tag{27}$$

where $P_l(\cos\theta)$ are the Legendre polynomials and dots denote time derivatives. In the case of a fluid source we have $H_2 = H_0$. The shear associated with the perturbations enters the stress-energy tensor via the anisotropic stress tensor

$$\delta\pi^b_a = -2\check{\mu}\delta s^b_a, \tag{28}$$

where $\check{\mu}$ is the shear modulus. We have assumed a Hooke-like relationship between the shear strain and stress. The total perturbed stress-energy tensor then takes the form

$$\delta T^{\rm tot}_{ab} = \delta T_{ab} + \delta\pi_{ab}, \tag{29}$$

which leads to significant alterations of the perturbation equations compared to the perfect fluid case. In order to deal with this, we define two new variables related to the traction. The radial traction, T_1, and the tangential traction, T_2, are defined by

$$T_1 = \delta\pi^r_r \quad \text{and} \quad T_2 = \delta\pi^\theta_r. \tag{30}$$

Both variables vanish in the perfect fluid case (as $\check{\mu} \to 0$). However, we will soon see that they are crucial in the implementation of the junction conditions at the crustal interfaces. The complete set of equations governing the perturbations in the elastic crust are lengthy and do not provide deeper insight into the dynamics. We therefore list them, together with their derivation, in Appendix A and mention only the key features here. The most notable difference between the two problems, key to including the extra elastic dynamical degrees of freedom, is the fact that the the metric perturbations H_0 and H_2 are no longer identical. Instead, we have

$$H_2 = H_0 + 64\pi\check{\mu}V\ , \tag{31}$$

where V is related to the tangential displacement (see Equation (13)).

Finally, let us consider possible phase-transitions in the star, which may come with a density discontinuity. Having derived the perturbation equations for the elastic crust, we need to connect the perturbations inside the crust to the perturbations for both the fluid core and the thin fluid ocean. This requires us to apply a set of interface conditions at each phase-transition. These conditions stem from the fact that the intrinsic curvature has to be continuous across the interfaces. This problem has already been analysed in detail [65, 67]. As our analysis is identical, we will simply state the relevant results here: At both crustal interfaces the continuity of the curvature imposes continuity of the perturbation variables H_0, H_1, K, W and T_2. In addition to the rather evident interfaces between the crust and the fluid, we have to pay attention to other possible phase-transitions. As explained in Section II B, the density profile inside a neutron star need not be continuous; phase-transitions at particular densities may cause density discontinuities. Such discontinuities cause the perturbation quantities to become discontinuous. However, it turns out that, as long as it is only the density that is discontinuous, we arrive at the same jump condition as for the crust-fluid interfaces (apart from the continuity of T_2 which is trivially given as $T_2 = 0$ in the fluid anyway). Furthermore, the Lagrangian pressure perturbation (the variable X, see Section III) is continuous across these interfaces.

III. NUMERICAL STRATEGY

The neutron star mode-problem requires the solution of a set of coupled first order differential equations, and the identification of solutions that represent purely outgoing gravitational waves at spatial infinity. The technical issues associated with this problem have been discussed in detail elsewhere, and the approach we take to the problem is relatively standard [1, 3, 5]. Our numerical strategy is conceptually the same as in several previous studies of polar oscillations, the closest being Lin et al. [12] where a three-layer star was considered. The essential difference is that the "middle" layer in their study was considered superfluid whereas in our case this layer forms the elastic crust. Nevertheless, we still have to deal with different sets of equations depending on whether a given layer is considered a perfect fluid or elastic and the junction conditions required to connect the layers.

We will outline the general idea for a specific case here and save a more technical description for Appendix C. We split the star into several layers, so that each layer requires one unique set of equations to be solved. Depending on the nature of each given layer, we have a certain number (in our case four or six) of independent variables. We start integrating the differential equations at one edge of the layer and continue to the other end; repeating this procedure with linearly independent initial vectors in order to achieve linearly independent solutions. This provides us with a basis that can be used to express the general solution to the problem. After doing this for all different layers in the star, we match the solutions at the interfaces. This leads to the need to solve a linear system for the "amplitudes" of the different solutions. The boundary conditions at the centre and the surface of the star finally determine one (up to amplitude) unique solution in the interior of the star. At the surface, we match the solution to the Zerilli function which is solved for outside the star and then calculate the amplitude of the ingoing wave amplitude at infinity, A_{in}. Whenever this amplitude is zero, we have found a quasinormal mode of the star.

The proposed approach has been used successfully in a number of previous studies [3, 4, 10], but as soon as we consider low-frequency oscillations we run into numerical difficulties. Undesirable noise in the low frequency part of the spectrum (higher order g-modes or thermal g-modes of old neutron stars as well as some of the i-modes would lie in this regime) prevents us from determining any oscillation modes in this regime. The problem is of purely numerical origin and mainly stems from the algebraic equation used to calculate the perturbation variable V (cf. Equation (A14) in [2]):

$$\omega^2 (\rho + p) V = e^{\nu/2} X + \frac{1}{r} p' e^{\nu - \lambda/2} W - \frac{1}{2} (\rho + p) e^{\nu} H_0, \tag{32}$$

where

$$X = -\frac{1}{r^l} e^{\nu/2} \Delta p. \tag{33}$$

A Taylor expansion (see [3]) reveals that all perturbation variables appearing in this equation, H_0, V, W and X, are of the same order of magnitude near the origin. The same is true for the coefficients on the right-hand side. As we are dealing with low frequencies, $\omega M \approx 0.001$ (say), the left-hand side of this algebraic relation forces the sum of the three terms on the right-hand side to be many orders of magnitude smaller than the sum's constituents, inevitably leading to numerical cancellation and hence inaccurate results.

This problem has already been addressed by Finn [5], who proposed a different set of equations for the study of low-frequency modes. His formulation makes use of the Eulerian pressure perturbation rather than the Lagrangian one. Such an implementation improves the accuracy of our results as the effect of the cancellation is not as severe; nevertheless, it does not fully satisfy our demands. Instead, we derive a new set of equations where the independent variables are a subset of the 'fundamental' variables, namely H_1, K, V and W. This formulation does not involve an algebraic equation like Equation (32) and thus the cancellation is avoided. The complete set of perturbation equations we use is given in Appendix B. The price we pay for eliminating the cancellation is the appearance of the derivative ρ' in the perturbation equations. Since this quantity is not known during the integration of the TOV equations, we have to calculate it numerically on an uneven grid; even worse, it may not be well-defined everywhere since $\rho(r)$ is not necessarily differentiable (density discontinuities may occur inside the star). We use the method proposed by Sundqvist & Veronis [68] to tackle the former problem. In order to overcome the latter, we only use this set of equations in a region near the origin up to a certain radius R_V, at which point the magnitude of the variables have changed sufficiently that Equation (32) can be applied without significant loss of accuracy and then switch back to the perfect fluid equations from [3]. This encourages a rather large value for R_V. However, when choosing R_V, we also have to ensure that there are no discontinuities in ρ inside the interval $[0, R_V]$ and furthermore, the calculation of ρ' suffers from (small but nevertheless present) numerical errors, which favours a small value for R_V. In the end, the 'optimal' value for R_V requires trial and error. In our calculations we find that $R_V \approx 5\,\text{km}$ is a good choice as it allows us to reliably extract mode frequencies down to $\approx 10\,\text{Hz}$ (the actual lower limit slightly depends on the problem under consideration, see Section IV). For different values of R_V, the numerical issues become more severe and in the

end the low frequency spectrum is contaminated by noise up to higher frequencies. Further work is needed on this problem.

IV. RESULTS

Since the spectrum of a relativistic star is rich, and could be difficult to untangle, we will build our understanding by taking the key bits of physics into account step by step. This will gradually enrich the spectrum with more and more classes of oscillation modes. The natural steps are: (i) taking only composition gradients into account, (ii) switching on temperature using the thermal evolution and (iii) accounting for the crystallisation of the elastic crust. The density jumps, leading to i-modes, are built-in to the EoS, so we cannot easily switch them on or off. Hence, these modes will always be present in the star's spectrum.

Let us briefly comment on the actual implementation of the density discontinuities. By far the easiest way of "implementing" them is to simply have them present in the tabulated EoS; for each discontinuity there are two adjacent lines in the given EoS with nearly (but not actually) identical values for the pressure but the density changes considerably. A TOV solver with adaptive mesh refinement will then lower the step size around these densities and the background model will have large gradients, ρ', at these densities. However, the phase-transitions do not appear as proper discontinuities here. It turns out that this is enough to find the interface modes in the spectrum. We also take a different approach to ensure that every phase-transition is reflected by an actual jump in density in our background model. For this, we modified the tabulated EoS by replacing the two pressure values for each phase-transition in the two adjacent lines by their average value. We also adjusted our TOV solver to ensure that two grid points are placed at each phase-transition; both with the same pressure but with the highest and lowest density of the discontinuitiy interval, respectively. When we compare these two implementations, we find that the frequencies of the interface modes with high frequencies are hardly changed while the interface modes with lower frequencies experience a serious shift.

It must be questioned which of these approaches is the most accurate. While the approach with actual discontinuities in density in the background model seems to be more sophisticated, it is certainly the case that a phase-transition in an actual neutron star occurs over a small but non-zero distance whereby the "simple implementation" is favoured. In our results, we opt for the "simple implementation" but we point out that a switch to the other case can be done quickly.

As in earlier work [3, 69], and since our focus is on oscillations that are slowly damped by gravitational-wave emission, we will not actually calculate the complex frequencies of the quasinormal modes; we ignore the damping of the mode. Instead, we construct the asymptotic amplitude A_{in} for real-valued frequencies and locate the quasinormal modes by approximating the zeros of this function (essentially resonances in the problem). To visualise the spectrum, we plot the logarithm of the incoming amplitude, $\log|A_{\text{in}}|$, as a function of the frequency (as in Figures 3, 5, 7 and 8); the logarithm turns the zeros into much more visible spikes and an eigenfrequency can be found where this function tends to $-\infty$. The damping times can also be estimated using this procedure [11] but we will not do so here. In fact, the damping times of (most of) the modes under consideration are so long, i.e. the imaginary part of ω is many orders of magnitude smaller than its real part, that a reliable calculation of the damping times would be impossible due to the finite machine precision.

We also comment here on the stability of our numerical procedure. As explained earlier, the calculation of the ingoing wave amplitude is spoilt by noise in the low frequency regime and, in practice, the lower limit for reliably extracting frequencies lies at about 15 Hz. In our simulations, we find that this lower limit gets shifted down to approximately 10 Hz when we include composition, i.e. when we use γ instead of γ_0 in the equations (see next subsection). This gives us a further hint to the origin of the instability in the equations. However, this is not the only crucial point since the noisy behaviour is almost non-existent for polytropic equations of state (which we implemented as a test of the numerics).

A. Composition Gradient

The first step beyond barotropic models involves including the composition gradient. Then we expect to find composition g-modes in the spectrum as well as i-modes due to the density discontinuities. The high frequency domain will be populated by f-modes and p-modes but we will not discuss this part of the spectrum much as it is well understood [3, 70]. Instead, we show the low frequency domain up to 250 Hz (as well as a zoom in at the lower end of the frequency window) for our neutron star model with zero temperature and without solid crust in Figure 3. This frequency range contains all low frequency modes in the model (above the noise cut-off). For comparison we show the spectrum for both the stratified star (solid line) and the corresponding unstratified star (dashed line). All

low-frequency modes in an unstratified star are i-modes due to density discontinuities and there is precisely one interface mode associated with each density discontinuity. We order them by frequency and label them as i_n ($n \geq 1$), where i_1 is the interface mode with the highest frequency.

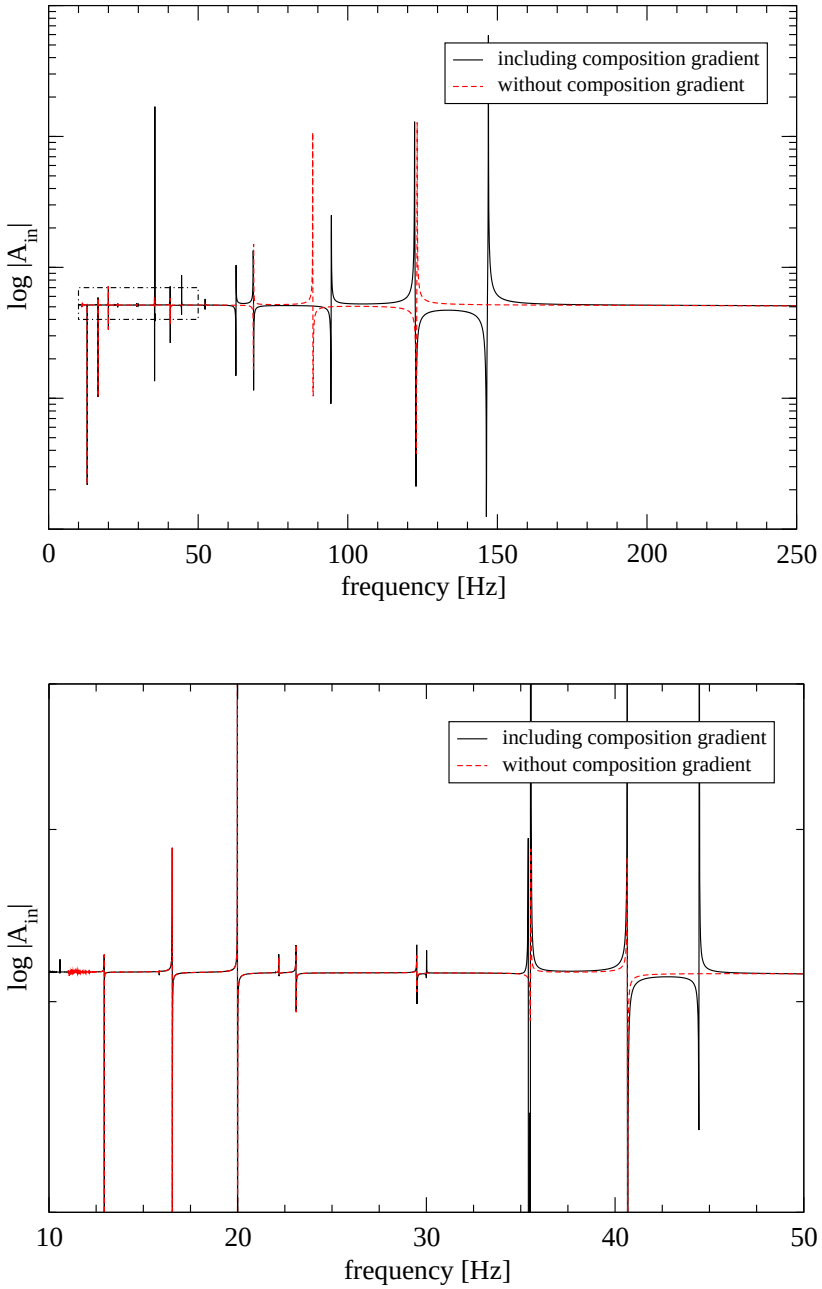

FIG. 3: The low frequency spectrum of our neutron star at zero temperature and without a solid crust. The upper panel shows the spectrum up to 250 Hz whereas the lower panel shows a magnification of the dash-dotted box. The dashed line shows the spectrum of the pure perfect fluid star, while the solid line includes composition gradients. All spikes in the dashed spectrum are interface modes as there is no composition gradient present; for each of these modes, there is also a mode present in the spectrum of the stratified star (with the exception of the mode at 88.4 Hz; see text). The "new" modes in the solid spectrum are composition g-modes.

It turns out that the association with interface modes and specific density discontinuities is not unambiguous. The general rule that the radial displacement of an interface mode has its peak amplitude exactly at the phase-transition does not hold in our case. The eigenfunctions do have their maximum at a phase-transition but we find that several interface modes would belong to the same phase-transition according to this procedure. Likewise, there are discontinuities at which none of the i-modes have a maximum there. This is the result of the presence of several

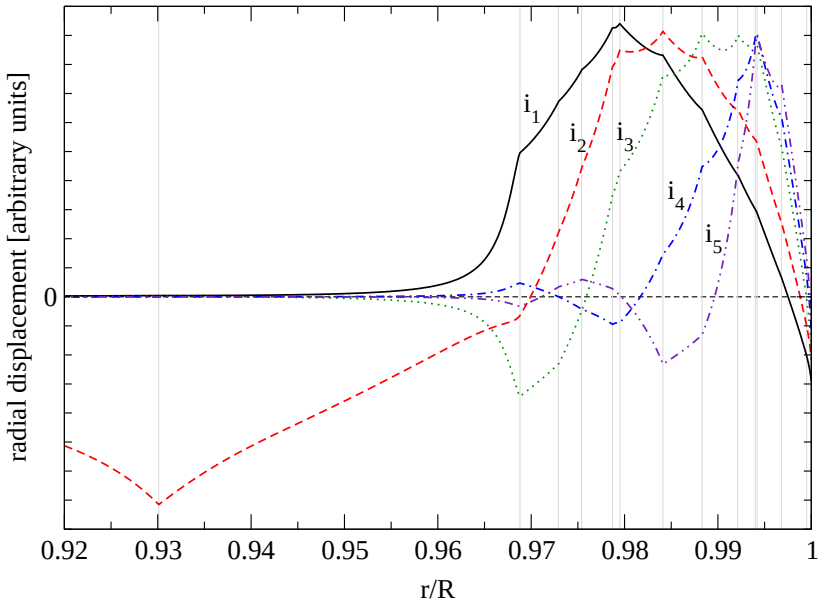

FIG. 4: The radial displacement, ξ^r, for five i-modes of the unstratified star. The vertical, grey lines show the location of the different density discontinuities within the star; the interface at $r/R \approx 93\,\%$ is the crust-core interface. The amplitudes of the different modes are scaled so that they are of comparable size. The kinks at the phase-transitions are clearly visible and the displacement nearly vanishes in the core (with the exception of the i_2-mode which is associated with the crust-core transition). The eigenfunction are largely unaffected if stratification is switched on (again with the exception of the i_2-mode which turns into a g-mode, see text).

discontinuities in close vincinity which affect each other. We show the eigenfunctions of five interface modes in Figure 4, where the kinks at the phase-transitions are clearly visible. The modes i_4 and i_5 have their strongest peak at the same transition. However, the i_1 mode has its highest amplitude at a transition where no other interface mode has its strongest peak. This suggests that this mode is associated with the transition $^{80}\mathrm{Zn} \to {}^{78}\mathrm{Ni}$. The i_2-mode apparently has its most prominent peak much deeper in the star and is associated with the artificial discontinuity at the crust-core interface due to the matching of the EoS.

Finn [6] provides a simple formula to give an estimate for the frequency of an i-mode; his calculations show that—in an idealised situation—the frequency of the interface mode is proportional to the relative jump in density, $\Delta\rho/\rho_+$, and the distance, Δr, of the associated phase-transition from the surface of the star. Even though our results qualitatively agree, the formula is, unfortunately, not accurate enough for our purposes to make the exact assocation. As mentioned above, we find that the mode i_1, which has the highest frequency amongst the interface modes in our star, is due to the transition $^{80}\mathrm{Zn} \to {}^{78}\mathrm{Ni}$. This transition has the largest relative jump in density of $\Delta\rho/\rho_+ \approx 4.3\,\%$ and is located rather deep in the star when compared to the other phase-transitions.

All interface modes (except for the one at 88.4 Hz; see below) are still present in the stratified star. However, we find a set of new modes appearing in the spectrum; these are the composition g-modes due to the stratification of the core (composition variations in the crust distinguish different layers and so only lead to interface modes associated with transitions from layer to layer). g-modes and i-modes are simple to distinguish if one examines their eigenfunctions. While the g-modes are mainly confined to the core and their radial displacement is a smooth function of the radius, the radial displacement of the i-modes nearly vanishes in the core and exhibit kinks at the phase-transitions (cf. Figure 4). In contrast to the i-modes, the set of g-modes is infinite and we label them as g_n, where g_0 is the g-mode with the highest frequency and n will correspond to the number of nodes of the radial displacement in the core.

Starting from the surface of the star, the 13th jump in density, which is due to the manual matching of the EoS at the crust-core interface, deserves a few more comments since no associated interface mode can be found in the stratified star. When the star is barotropic (not stratified), we find an i-mode at 88.4 Hz associated with this density discontinuity. As this discontinuity lies within (or at least at the edge of) the region where we account for stratification and an interface mode can be understood as a special kind of composition g-mode (a sudden change in density indicates a phase-transition and as a result, a perturbed fluid element crossing this interface will experience buoyancy due to the different composition), this i-mode loses its character and turns into the g-mode of lowest order when the star is stratified. To verify this, we ran a series of separate simulations in which we slowly increased the composition gradient via the adiabatic index γ from "no stratification" up to "full stratification" (as given in the EoS). The interface mode

accordingly increased in frequency and its eigenfunction changed, turning into the g_0 mode of the stratified star. This example illustrates the close relationship between the two classes of modes.

We list the low frequency modes of the stratified star in Table I. The spectrum of the barotropic star can be easily extracted from this table by the following procedure: Remove all g-modes from this table and add one i-mode at 88.4 Hz. The frequencies of the i-modes are barely affected by stratification (they vary only by a few tenths of a Hertz).

TABLE I: Frequencies of the i-modes and composition g-modes in the stratified, cold star.

Frequency [Hz]	Mode	Frequency [Hz]	Mode
146.4	g_0	30.0	g_5
122.8	i_1	29.5	i_6
94.4	g_1	25.5	g_6
68.5	i_2	23.1	i_7
62.6	g_2	22.2	i_8
52.3	i_3	22.0	g_7
44.4	g_3	20.0	i_9
40.7	i_4	16.5	i_{10}
35.6	i_5	15.8	i_{11}
35.4	g_4	12.9	i_{12}

B. Finite Temperature

The next step is to move away from the assumption that the neutron star is cold. As we have already described, we account for the thermal pressure by adding it to the static pressure of the cold equation of state used to determine the background. This leads to the results shown in Figure 5, which shows the low frequency spectrum of an isothermal neutron star with temperature $Te^{\nu} = 10^{10}$ K (our initial configuration). In comparison to the result at zero temperature (cf. Figure 3), we find a vastly enriched spectrum. A careful investigation reveals that all composition g-modes found in the cold, stratified star are still present in the hot star at only marginally altered frequencies (the difference is generally less than 0.1%, only the high freqency g-modes are shifted by up to 4%); likewise their eigenfunctions are unaltered. This is as expected since the composition g-modes in our model originate from the composition gradient in the core. The thermal pressure, however, is negligible in the core and hence does not affect the g-modes.

For the i-modes the situation is somewhat different. We find all interface modes in the hot star, too; however, while the low frequency interface modes maintain their frequency throughout the thermal evolution of the star, four interface modes with high frequencies (i_1, i_2, i_4 and i_5) have their oscillation period increased. We are unable to provide a reason as to why this behaviour is observed for precisely these interface modes but not others.

In order to track the evolution of the spectrum as the star ages, we produced a time evolution of the low frequency modes in the following way: We start with the isothermal star at $Te^{\nu} = 10^{10}$ K, for which the spectrum is that shown in Figure 5, and extract temperature profiles at 120 time steps uniformly distributed on a logarithmic timescale. After extracting the mode frequencies for each of these temperature profiles, we are able to trace the evolution of the oscillation modes over time. This leads to the results shown in Figure 6. All modes exhibit avoided crossings which are easily visible in the high frequency part of the graph; they are also present in the low frequency part, where a higher resolution is necessary to resolve the different modes.

We now find a set of new modes spread over the entire spectrum; these are the thermal g-modes. Their frequency decreases as the star cools and after about 10 years nearly all the thermal g-modes have frequencies of 15 Hz or less. This is when the temperature has decreased so far that the thermal pressure is almost negligible and does not affect the frequencies of the g- and i-modes anymore.

For completeness, we considered the impact of thermal pressure on the fundamental and pressure modes. As an illustration of the results, we show the star's spectrum after 10 seconds, one month and 100 years in Figure 7. Since the f-mode is mainly due to the surface of the star and depends on the average density, it does not change (especially since we do not account for thermal pressure in the background model). The p-modes, however, should be affected since the thermal pressure contributes to the restoring force acting on sound waves. In our simulations we observe a slight increase in frequency by up to roughly 5 %, but only for p-modes of higher order and only in young, hot neutron

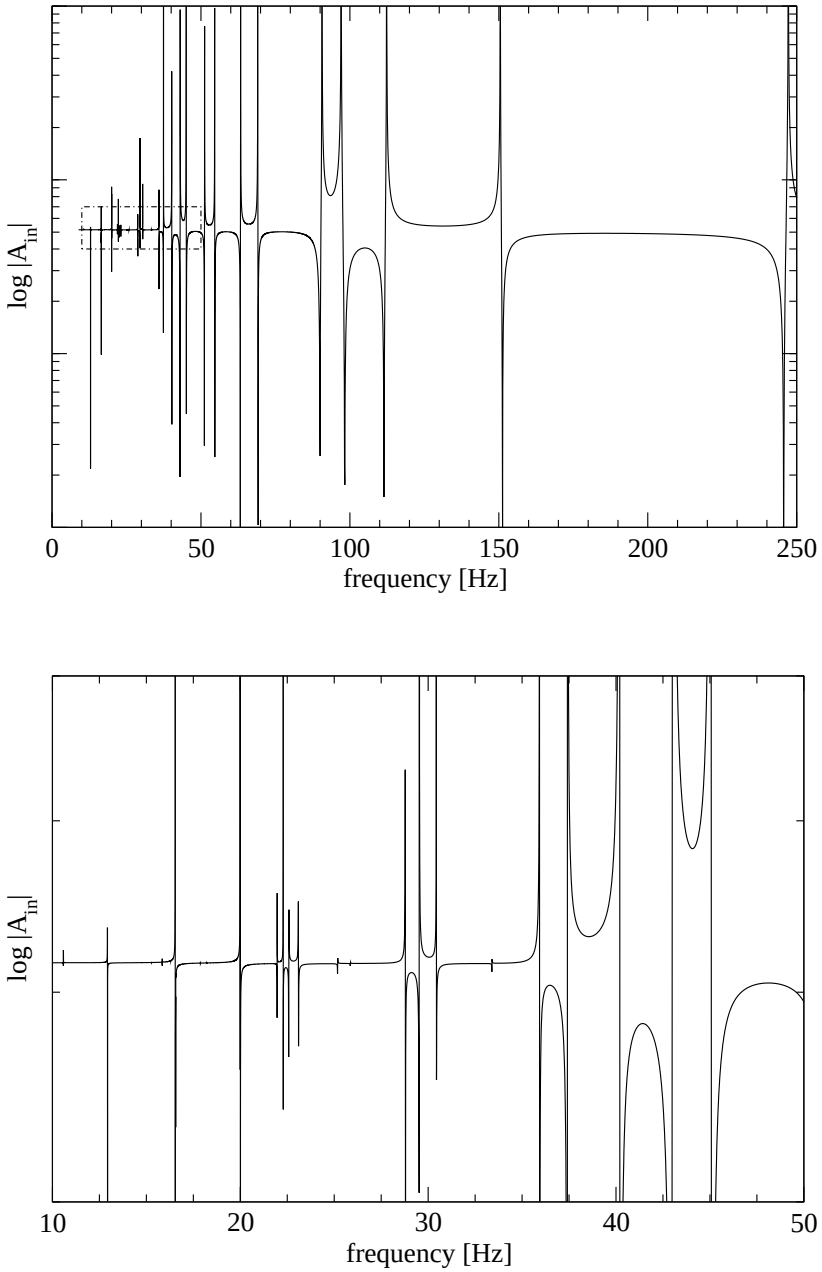

FIG. 5: The low frequency spectrum when the star is 3 seconds old; including thermal pressure but without solid crust. The lower panel shows a magnification of the dash-dotted box in the upper panel.

stars. As is apparent from Figure 7, after just one month the frequencies of the p-modes are no longer affected by the thermal pressure.

C. The Crust Elasticity

Finally, we add the elastic crust to the model. As explained in Section II D, we define the region in which the crust is solid via the condition $\Gamma > 173$ for the Coulomb coupling parameter. As in the previous Section, we start from an isothermal star with $Te^{\nu} = 10^{10}\,\mathrm{K}$. At this point, the star already has a thin crust, spanning the region from 10.94 km to 11.36 km, cf. Figure 2. In Figure 8 we show the spectrum up to 8 kHz for this model, including the thermal pressure and composition gradients. The lower panel in Figure 8 provides a zoom-in at low frequencies. The two most prominent oscillation modes at 1.938 kHz and 6.316 kHz are the f-mode and the first p-mode, respectively;

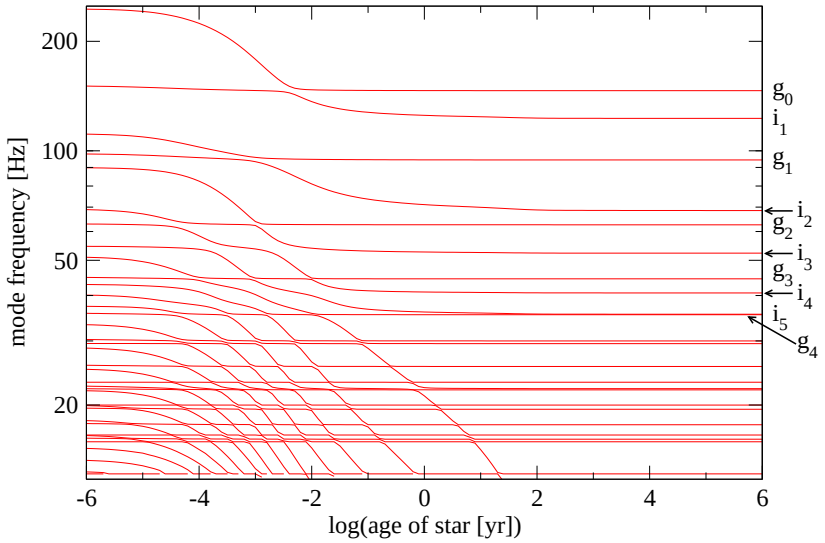

FIG. 6: The star's low-frequency spectrum as the star cools. The thermal g-modes quickly decrease in frequency and are below 15 Hz after about 10 years. Four of the high frequency interface modes are affected by the thermal pressure (i_1, i_2, i_4 and i_5). All modes clearly exhibit avoided crossings.

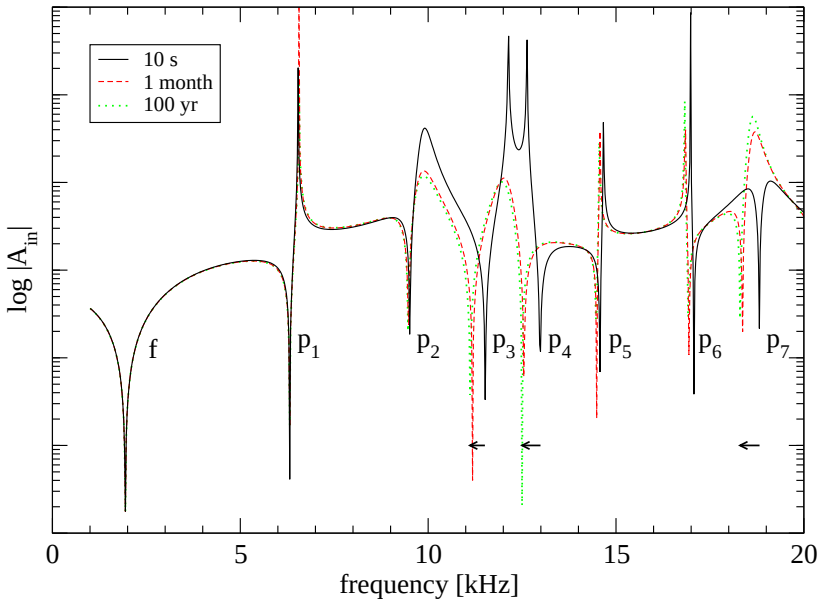

FIG. 7: The stellar spectrum up to 20 kHz for three different temperature profiles. Clearly visible are the f-mode and first 7 p-modes. Where the frequency of a p-mode varies visibly over time, an arrow indicates this change.

see also Figure 7. As expected, they are unaffected by the presence of the solid crust.

The low frequency domain again shows evidence for a large set of oscillation modes. However, only very few modes have maintained their frequency compared to the perfect fluid star. This is not surprising as we have changed the physics of the crust considerably and all the interface modes stem from phase-transitions within the crust. The thermal pressure has a smoothing effect on the spectrum. As the star cools, the entire spectrum becomes gradually spoilt by noise which makes it very difficult to extract the eigenfrequencies. For this reason, we are unable to trace the low frequency modes along the entire thermal sequence and we cannot compare the spectra of the cold stars (which would be easier since the number of modes is considerably lower due to the lack of thermal g-modes). Once the reason for this noise has been found, a more precise analysis of the low frequency spectrum of the star with an elastic crust will be possible.

When we consider higher frequencies, we find several narrow spikes in the spectrum. These belong to the shear

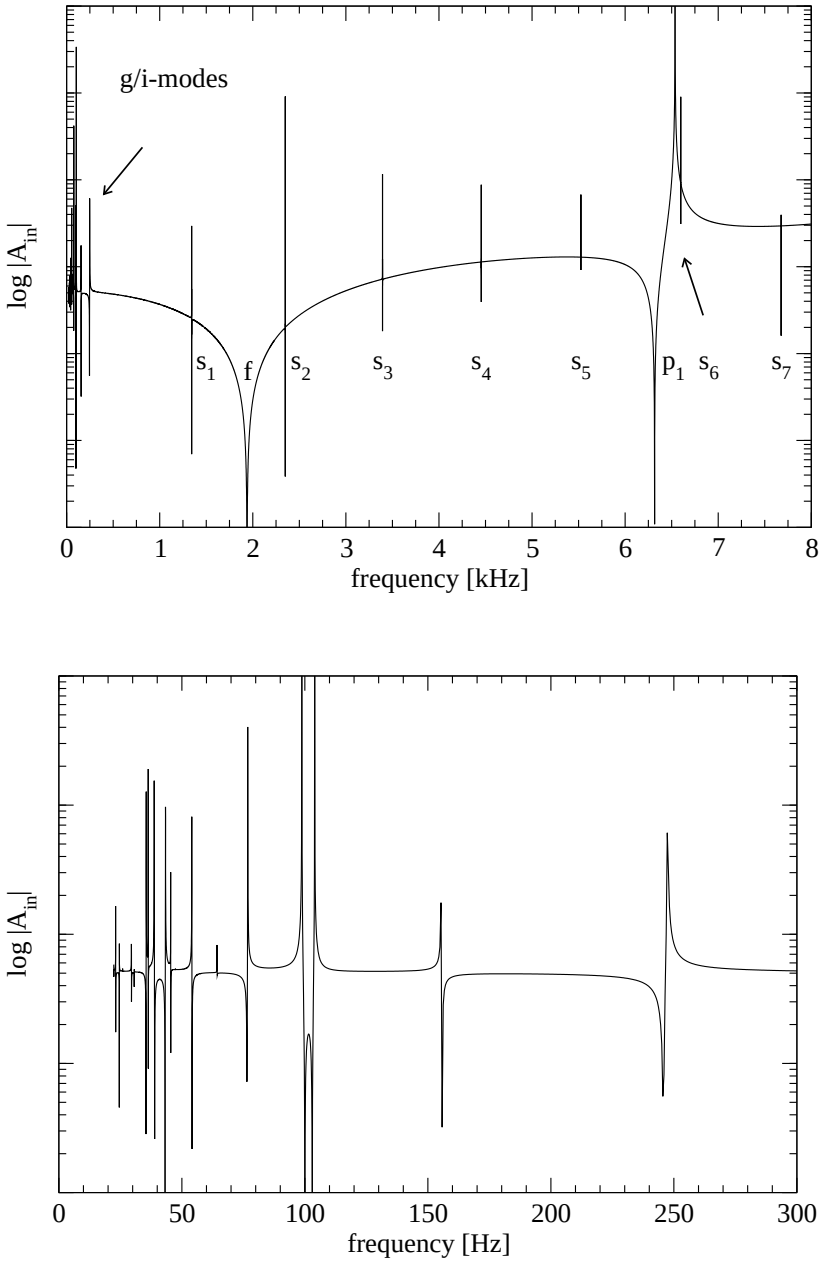

FIG. 8: The spectrum of our model star including thermal pressure and an elastic crust, after three seconds of the star's life. The upper panel shows the high frequency domain, while the lower panel zooms in at low frequencies to resolve the g- and i-modes.

modes associated with the solid crust. We list the frequencies of the seven lowest shear modes at the beginning of our cooling sequence in Table II. In Figure 9, we show the radial and transverse displacement of the second shear mode s_2; we denote shear modes by s_n where n corresponds to the order of the oscillation. Note that we have scaled the transverse displacement, represented by the variable V, by a factor of 0.02. That is, the displacement is predominantly transverse. Furthermore, the displacement is strongly confined to the crust (apart from a small, almost constant, radial displacement in the fluid ocean). Both displacement variables exhibit one oscillation to very good precision; however, they are out of phase by approximately $\pi/4$ which indicates an ellipsoidal motion (rather than circular due to the dominance of the transverse displacement) of the "fluid elements" in the crust. The eigenfunctions for the other shear modes show a similar behaviour; higher order shear modes exhibit more oscillations, in particular, the number of oscillations increases by one half per order.

The frequency of the shear waves deserves a further comment. At the beginning of our cooling sequence, the star

TABLE II: Frequencies of the shear modes for the neutron star model at the beginning of our cooling sequence. The redshifted temperature of the star at this time is 10^{10} K.

Frequency [kHz]	Mode
1.343	s_1
2.349	s_2
3.394	s_3
4.455	s_4
5.525	s_5
6.598	s_6
7.676	s_7

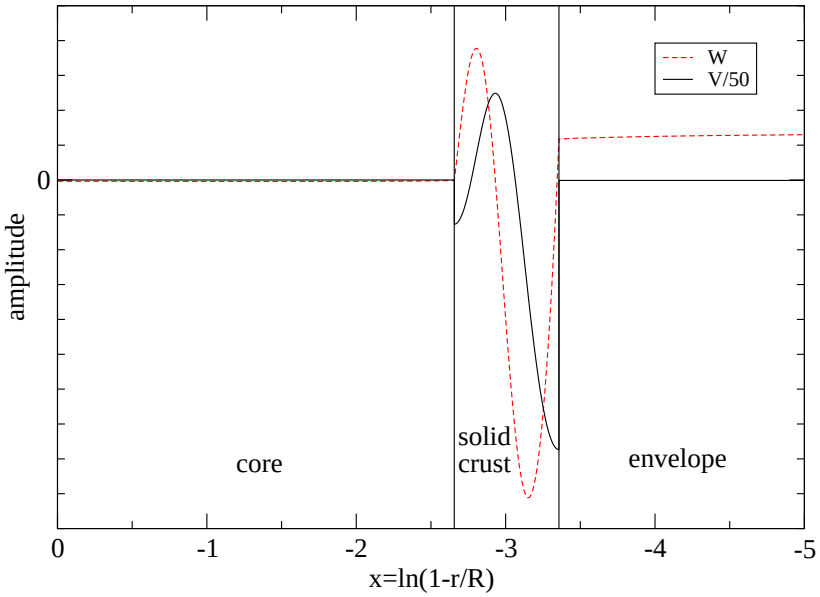

FIG. 9: The displacement associated with the second shear mode, s_2.

has a solid crust in the region from $R_{cc} = 10.94\,\mathrm{km}$ (**c**ore-**c**rust interface) to $R_{co} = 11.36\,\mathrm{km}$ (**c**rust-**o**cean interface). As is apparent from Figure 9, the s_2 mode essentially fits one oscillation into this region, suggesting a wavelength of $\lambda \approx 420\,\mathrm{m}$. This is the same behaviour as observed for axial shear modes [23]. Together with the frequency of 2.349 kHz we infer a wave speed of $c = \lambda f \approx 10^8\,\mathrm{cm/s}$. This is in very good agreement with the shear velocity $c_t = \sqrt{\hat{\mu}/\rho}$, which varies between $0.98 - 1.4 \times 10^8\,\mathrm{cm/s}$ in the elastic region (as calculated from values provided by the DH EoS). This is, of course, as it should be.

In Figure 10 we show how the high frequency part of the spectrum changes with time. We can identify the two frequencies, 1.938 kHz and 6.316 kHz, which are eigenfrequencies of the star during its entire lifetime (apart from very short periods when a shear mode crosses over and the two modes in question exhibit an avoided crosssing); these are the f-mode and the first p-mode, respectively. The lowest frequency mode in the figure, the first shear mode s_1, seems to be constant over time but in fact decreases slightly with time. The global f- and p_1-modes, are affected neither by the formation of the crust nor by the thermal pressure. All other modes in this figure are shear modes which are purely due to the existence of the elastic crust. As explained above, we expect their frequencies to be determined roughly by the shear speed and the thickness of the crust. Since the crystallised region grows as the star cools while the shear speed is subject to only small variations, we expect the shear mode frequencies to decrease with time. This effect is clearly visible, the most prominent drop in frequency happening after about $2 \times 10^{-4}\,\mathrm{yr} \approx 2\,\mathrm{h}$ when the solid crust grows in width very quickly (cf. Figure 2). This is due to the fact that the melting temperature has a rather small gradient and hence the crust will crystallise in a sizeable region almost at the same time. In Figure 10, this drop appears to be almost discontinuous. A second prominent drop in frequency occurs after about $3.2 \times 10^{-2}\,\mathrm{yr} \approx 1\,\mathrm{week}$ and lasts for almost one year. The frequencies are continuously decreasing as the star cools over time, hence forcing the crust to solidify. After roughly one year, the maximum temperature throughout the star is about $10^9\,\mathrm{K}$ and the

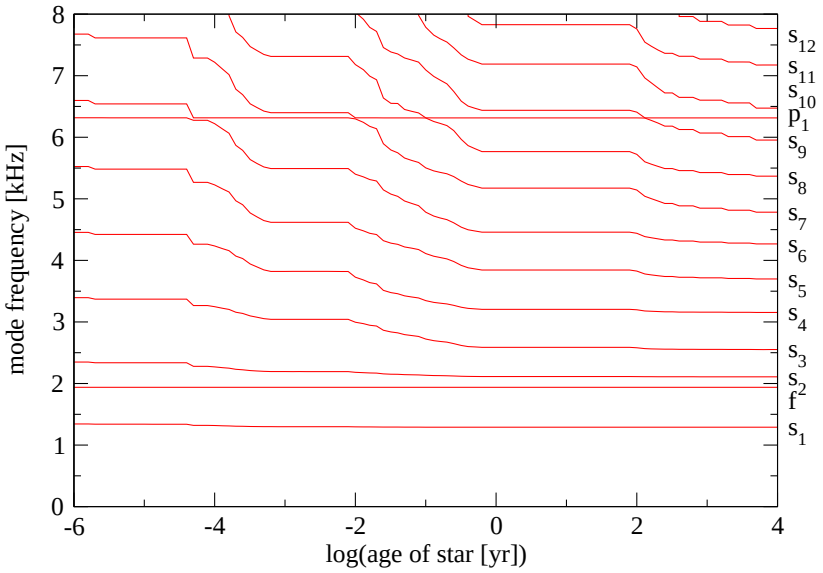

FIG. 10: Same as Figure 6 but this time for the high frequency part of the spectrum, where our model star accounts for the elastic crust. The results show how the mode frequencies change as the star cools. The two constant frequencies at 1.938 kHz and 6.316 kHz are the f-mode and first p-mode, respectively, whose frequencies remain unaffected.

solid crust has almost reached its final thickness. Thus, the shear modes do not experience a significant change in frequency later.

Our findings for stratified stars with an elastic crust are in agreement with results from McDermott et al. [71] who considered a star with an elastic crust in Newtonian theory. Qualitatively, our numerical calculations confirm their spectra; we find the same sets of mode, that is f-, p-, g-, i- and s-modes. However, while McDermott et al. find two different sets of g-modes which they label surface g-modes and core g-modes, according to the region to which they are mainly confined, our simulations do not reproduce these findings as we do not have a detailed ocean model here. Furthermore, the frequencies for the g-modes which McDermott et al. find are much lower (below 3 Hz) than in our simulations. This is due to the rather low temperature (10^7 K) used in their calculations. At these temperatures we would expect similar frequencies in our simulations but the numerical procedure does not allow us to investigate the spectrum at these low values. Nevertheless, our results agree qualitatively with the results of McDermott et al. [71].

V. SUMMARY AND CONCLUSIONS

The aim of this paper was to establish a formalism that allows us to study neutron star oscillations in full general relativity, accounting for as much realistic microphysics as possible. So far we extended the standard perfect fluid formalism to account for thermal pressure in the star's core and derived a new set of equations which govern perturbations in the solid crust. We provided sample results for a realistic equation of state. However, the equation of state is not consistent yet: the core and the crust equation of state were matched manually. This does not present a problem since we can consider the equation of state to be another parameter, and once a consistent equation of state is provided it can be used in our numerical code pretty much straightaway.

We focus our attention on the low-frequency part of the oscillation spectrum (above 15 Hz or so due to computational limitations). In this regime we find a set of interface modes, firstly due to the (artificial) density discontinuity at the crust-core interface and secondly there are interface modes associated with the crust region, due to sharp changes in the low-density equation of state. The composition gradient in the core shifts the frequency of the artificial interface mode to slightly higher frequencies, and we find a set of composition g-modes in the low frequency regime. The frequencies of these g-modes are slightly lower than previous literature values—this is because the composition gradient is rather small throughout nearly the entire core; only close to the crust-core transition is the composition gradient reasonably pronounced.

When we account for thermal pressure due to neutrons and protons in the core, we find that a number of thermal g-modes enter the low frequency part of the spectrum. Meanwhile, the high frequency interface modes are shifted to even higher frequencies whereas the composition g-modes stay unaffected. Tracking the thermal evolution of the neutron star for the first few hundred years, we investigate how the frequencies of the various modes evolve as the star

matures through adolescence. After approximately 10 years, all thermal g-modes have dropped below 15 Hz and the thermal effect on the interface modes has almost vanished entirely. During the next 100 years, as the star continues to cool, the frequencies of the interface modes change slightly, finally leaving us with the spectrum of a cold star. Note that our analysis did not account for thermal pressure in the crust, a feature one might want to add in future studies.

Finally, we considered the crystallization of the crust and investigated the associated changes in the spectrum. From our thermal evolution, we determined the solid region in the outer parts of the star. We quantified how the crust elasticity affects the interface modes associated with the outer layers of the star, and discussed how the spectrum is enriched by shear modes. As expected, our results for the shear modes are in good agreement with results from previous work [71].

In summary, we have taken the first step towards a comprehensive computational technology to study quasinormal modes of realistic compact stars. We plan to extend the model to account for a multifluid core where the neutrons are superfluid and the protons are superconducting. In doing so we will consider recent equation of state data, in particular concerning the entrainment effect, both in the core and the crust. We will also update the cooling sequence to account for superfluid effects. We expect to report on results in these directions in the not too distant future.

VI. ACKNOWLEDGEMENTS

We are grateful to Ian Hawke and Ian Jones for helpful discussions. CJK acknowledges the use of the IRIDIS High Performance Computing Facility, and associated support services at the University of Southampton, in the completion of this work. WCGH appreciates the use of the computer facilities at the Kavli Institute for Particle Astrophysics and Cosmology. CJK acknowledges financial support from the Engineering and Physical Sciences Research Council (EPSRC) and the School of Mathematics at the University of Southampton. NA and WCGH acknowledge support from the Science and Technology Facilities Council (STFC) in the United Kingdom.

Appendix A: Polar Perturbation Equations for the Elastic Crust

The perturbations are governed by the linearised Einstein equations and the conservation laws for the matter:

$$\delta G_{ab} = 8\pi \delta T_{ab} \quad \text{and} \quad \delta\left(\nabla_a T^{ab}\right) = 0, \tag{A1}$$

where δT^{ab} denotes the *total* stress-energy tensor as given in Equation (29). In addition, we have definitions of the two traction variables, T_1 and T_2, which in their expanded form read

$$T_1 = \frac{4}{3}\check{\mu}\left[e^{-\lambda/2}(2l-4)W + 2re^{-\lambda/2}\frac{\partial W}{\partial r} + r^2(K-H_2) - l(l+1)V\right], \tag{A2}$$

$$T_2 = -2\check{\mu}\left[e^{\lambda/2}W - (l-2)V - r\frac{\partial V}{\partial r}\right]. \tag{A3}$$

As in the perfect fluid case [2], we use the Lagragian variation of the pressure as an independent variable

$$X = -\frac{1}{r^l}e^{\nu/2}\Delta p = \frac{\gamma p}{r^2}e^{\nu/2}\left[e^{-\lambda/2}(l+1)W + re^{-\lambda/2}\frac{\partial W}{\partial r} - r^2(K+\frac{1}{2}H_2) + l(l+1)V\right]. \tag{A4}$$

For brevity and clarity, we have suppressed the angular dependence in all these relations.

If we define

$$Q = \frac{1}{2}r^2 e^{-\lambda}\nu' \ , \tag{A5}$$

and

$$m = \frac{1}{2}(l+2)(l-1) \ , \tag{A6}$$

and make liberal use of Equations (5), (6), (7) and (8), the full set of perturbation equations for the elastic crust

reads:

$$\frac{\partial H_1}{\partial r} = \left[\frac{1}{2}(\lambda' - \nu') - \frac{l+1}{r}\right] H_1 + \frac{e^{\lambda}}{r}\left[H_2 + K - 16\pi(\rho + p)V\right] \tag{A7}$$

$$\frac{\partial K}{\partial r} = \frac{1}{r}H_2 + \frac{m+1}{r}H_1 + \left(\frac{1}{2}\nu' - \frac{l+1}{r}\right)K - \frac{8\pi(\rho+p)e^{\lambda/2}}{r}W, \tag{A8}$$

$$\frac{\partial H_0}{\partial r} = +\frac{\partial K}{\partial r} - re^{-\nu}\omega^2 H_1 - \left(\frac{1}{2}\nu' + \frac{l-1}{r}\right)H_0 - \left(\frac{1}{2}\nu' + \frac{1}{r}\right)H_2 + \frac{l}{r}K - \frac{16\pi}{r}T_2, \tag{A9}$$

$$\frac{\partial W}{\partial r} = -\frac{l+1}{r}W + re^{\lambda/2}\left[\frac{e^{-\nu/2}}{\gamma p}X - \frac{l(l+1)}{r^2}V + \frac{1}{2}H_2 + K\right], \tag{A10}$$

$$\frac{\partial V}{\partial r} = \frac{1}{2\check{\mu}r}T_2 + \frac{e^{\lambda/2}}{r}W + \frac{2-l}{r}V, \tag{A11}$$

$$\begin{aligned}\frac{\partial T_2}{\partial r} = &-\frac{1}{2}re^{\lambda}(\rho+p)H_0 + re^{\lambda-\nu/2}\left(X - \frac{1}{2r^2}e^{\nu/2}T_1\right) + \left[\frac{1}{2}(\lambda'-\nu') - \frac{l+1}{r}\right]T_2 \\ &+ \left[\frac{4me^{\lambda}\check{\mu}}{r} - e^{\lambda-\nu}r\omega^2(\rho+p)\right]V + e^{\lambda/2}p'W.\end{aligned} \tag{A12}$$

In addition to these six ordinary differential equations (ODEs), we have three algebraic relations:

$$H_2 = H_0 + 64\pi\check{\mu}V, \tag{A13}$$

$$\begin{aligned}(2M + Q + mr)\,H_0 = &\,8\pi r^3 e^{-\nu/2}X - \left[(m+1)Q - \omega^2 r^3 e^{-(\lambda+\nu)}\right]H_1 \\ &+ \left[mr - \omega^2 r^3 e^{-\nu} - \frac{e^{\lambda}}{r}Q(2M+Q-r)\right]K \\ &+ 8\pi r T_1 - 16\pi r e^{-\lambda}T_2,\end{aligned} \tag{A14}$$

$$\frac{2}{3}e^{-\nu/2}\check{\mu}r^2 X - \frac{1}{4}\gamma p T_1 = \check{\mu}\gamma p\left[2e^{-\lambda/2}W - r^2 K + l(l+1)V\right]. \tag{A15}$$

The origin of the equations are (for brevity, we denote the components of the Einstein equations with $[ab]$ as a shortcut for $G_{ab} = 8\pi T_{ab}$): Equations (A7), (A8) and (A9) are $[t\theta]$, $[tr]$ and $[r\theta]$, respectively; (A10) and (A11) are due to the definitions of X and T_2, respectively; (A12) is $\delta\left(\nabla_a T^a_\theta\right) = 0$; (A13) is the difference $[\theta\theta] - [\phi\phi]$; (A14) is $[rr]$ and (A15) is obtained by removing $\partial_r W$ from the definitions of X and T_1.

Appendix B: Low-Frequency Equations

In the low-frequency domain, we need to circumvent numerical difficulties arising from an algebraic equation in the 'standard formulation' of the perfect fluid problem. This led us to using V instead of X as an independent variable. The perturbation equations for this set of variables then take the form

$$\frac{\partial H_1}{\partial r} = \left[+\frac{1}{2}\left(\lambda' - \nu'\right) - \frac{l+1}{r}\right]H_1 + \frac{e^{\lambda}}{r}\left[H_0 + K - 16\pi\left(\rho + p\right)V\right], \tag{B1}$$

$$\frac{\partial K}{\partial r} = \frac{1}{r}H_0 + \frac{m+1}{r}H_1 + \left(\frac{1}{2}\nu' - \frac{l+1}{r}\right)K - \frac{8\pi\ (\rho+p)}{r}e^{\lambda/2}W, \tag{B2}$$

$$\frac{\partial W}{\partial r} = -\left(\frac{l+1}{r} + \frac{p'}{F}\right)W + re^{\lambda/2}\left[\frac{\rho+p}{F}\left(e^{-\nu}\omega^2 V + \frac{1}{2}H_0\right) - \frac{l(l+1)}{r^2}V + \frac{1}{2}H_0 + K\right], \tag{B3}$$

$$\begin{aligned}\frac{\partial V}{\partial r} = &\left(\frac{p'}{F} - \frac{\rho'}{\rho+p} + \nu' - \frac{l}{r}\right)V + \frac{1}{2\omega^2}e^{\nu}\left(\frac{p'}{F} - \frac{\rho'}{\rho+p}\right)\left(H_0 + \frac{1}{r}e^{-\lambda/2}\nu' W\right) \\ &+ rH_1 - \frac{1}{r}e^{\lambda/2}W,\end{aligned} \tag{B4}$$

where we have introduced the abbreviation

$$F = \gamma p + n_{\rm n}\frac{\partial p^{\rm n}_{th}}{\partial n_{\rm n}} + n_{\rm p}\frac{\partial p^{\rm p}_{th}}{\partial n_{\rm p}}. \tag{B5}$$

The Einstein equations imply the following algebraic relation between the perturbation variables, which we use in order to calculate H_0:

$$\begin{aligned}\left[3M - 4\pi r^3\rho + mr\right] H_0 = &- \left[(m+1)Q - \omega^2 r^3 e^{-(\lambda+\nu)}\right] H_1 \\ &+ \left[mr - \omega^2 r^3 e^{-\nu} - \frac{e^\lambda}{r} Q(2M + Q - r)\right] K \\ &+ 8\pi e^{\lambda/2} Q(\rho + p) W + 8\pi r^3 e^{-\nu}\omega^2 (\rho + p) V,\end{aligned} \tag{B6}$$

The origin of the equations is basically the same as in previous work, but still deserves a few comments. In order to arrive at our set of equations, we start from the Detweiler & Lindblom set of equations [3]. Since the algebraic relation (32) causes numerical problems, we solve it for X and substitute into the other equations. After some algebraic manipulations and making use of the background equations as well as the other perturbation equations, we then arrive at our set of perturbation equations.

Equations (B1), (B2) and (B6) follow from $[t\theta]$, $[tr]$ and $[rr]$ of the perturbed Einstein equations, respectively; (B3) is due to the definition of (the no longer appearing) X; (B4) is $\delta(\nabla_a T^a_r) = 0$ and (32), which has been used as an auxiliary equation only, is $\delta(\nabla_a T^a_\theta) = 0$.

Before we can solve Equation (B6) for H_0, we have to assure that its coefficient is non-singular at any point. This is easy to see, as we have

$$3M = 3\int_0^r 4\pi r'^2 \rho(r') dr' \geq 3\int_0^r 4\pi r'^2 \rho(r) dr' = 4\pi r^3 \rho, \tag{B7}$$

where we used Equation (5) for the first equality and monotonicity of the density inside the star for the estimate. Thus, the coefficient will be singular only at the origin, $r = 0$, where we use a Taylor expansion anyway.

1. Behaviour at the Origin

Since the perturbation equations (see Equations (B1) - (B6)) are singular at the origin due to the use of spherical coordinates, we expand all variables by Taylor series near the origin, $r = 0$. For all our perturbation variables H_0, H_1, K, V and W, we use an expansion of the form

$$Q(r) = Q_0 + \frac{1}{2} r^2 Q_2 + \mathcal{O}\left(r^4\right). \tag{B8}$$

The field equations imply that the first order corrections vanish. The zeroth order constraints imposed by the perturbation equations are

$$H_{10} = \frac{2lK_0 + 16\pi(\rho_0 + p_0) W_0}{l(l+1)}, \qquad V_0 = -\frac{1}{l} W_0, \qquad H_{00} = K_0, \tag{B9a}$$

which demonstrates that, once K_0 and W_0 are chosen, the remaining expansion coefficients, H_{00}, H_{10} and V_0 are determined. Here and in the following, we need the expansion coefficients of the background quantities, ν, λ, p and ρ as well. We expanded them in the same way as specified in Equation (B8); their second order coefficients are given by

$$\lambda_2 = \frac{16}{3}\pi\rho_0, \tag{B10}$$

$$\nu_2 = \frac{8}{3}\pi(\rho_0 + 3p_0), \tag{B11}$$

$$p_2 = -\frac{1}{2}\nu_2(\rho_0 + p_0), \tag{B12}$$

$$\rho_2 = \frac{p_2(\rho_0 + p_0)}{\gamma p_0}. \tag{B13}$$

The second order coefficients of the perturbation variables are then given by the following linear system:

$$-\frac{l+3}{2}H_{12}+\frac{1}{2}K_2-8\pi(\rho_0+p_0)V_2+\frac{1}{2}H_{02}$$
$$=\frac{1}{2}(\nu_2-\lambda_2)H_{10}-\lambda_2K_0+8\pi\left[\rho_2+p_2+\lambda_2(\rho_0+p_0)\right]V_0, \tag{B14a}$$
$$\frac{m+1}{2}H_{12}-\frac{l+3}{2}K_2-4\pi(\rho_0+p_0)W_2+\frac{1}{2}H_{02}$$
$$=-\frac{1}{2}\nu_2K_0+2\pi\left[2(\rho_2+p_2)+\lambda_2(\rho_0+p_0)\right]W_0, \tag{B14b}$$
$$-(m+1)F_0V_2-\frac{l+3}{2}F_0W_2$$
$$=-\frac{1}{2}\left(3F_0+p_0+\rho_0\right)K_0+\left[\frac{m+1}{2}\lambda_2F_0-lp_2-e^{-\nu_0}\omega^2(\rho_0+p_0)\right]V_0, \tag{B14c}$$
$$(l+2)V_2+W_2 = 2H_{10}-\frac{e^{\nu_0}}{\omega^2}\left(\frac{\rho_2}{\rho_0+p_0}-\frac{p_2}{F_0}\right)K_0$$
$$+\left[\frac{l}{2}\lambda_2+2\nu_2+\left(2-\frac{le^{\nu_0}\nu_2}{\omega^2}\right)\left(\frac{p_2}{F_0}-\frac{\rho_2}{\rho_0+p_0}\right)\right]V_0, \tag{B14d}$$
$$\frac{m}{2}K_2-\frac{m}{2}H_{02} = \left(\frac{m+1}{2}\nu_2-\omega^2e^{-\nu_0}\right)H_{10}+\left(\omega^2e^{-\nu_0}-\frac{1}{2}\nu_2\right)K_0$$
$$-8\pi e^{-\nu_0}\omega^2(\rho_0+p_0)V_0+8\pi p_2W_0. \tag{B14e}$$

Appendix C: Numerical Strategy - General Case

Here, we describe the details of the numerical procedure for the interior solution. In this work, we consider a star with three layers. However, as more physics are taken into account, we will have to slice the neutron star into more layers, each of which extends over a region in which the neutron star matter is homogeneous in the sense that it can be described by the same set of equations. Thus, in anticipation of extending our work to account for superfluidity, where we will certainly have more than three distinct regions within the star, we consider a star with n layers. The same procedure with exactly the same underlying idea and very similar junction conditions has already been explained in great detail for a three-layer star by Lin et al. [12]. Hence, using this n-layer description and applying it to our 3-layer star together with the junction conditions from Section II E is straightforward.

As an example, consider a neutron star which consists of n layers. The interfaces between the layers, including the center and the surface of the star, are at the radii $0 = R_0 < R_1 < R_2 < \cdots < R_{n-1} < R_n = R$, where R is the star's radius. Within each of the different layers, the dynamics and the perturbations, respectively, are governed by a certain set of equations which obviously depends on the nature of the matter within this region. It could be, for instance, a perfect fluid, the elastic crust or a superfluid. We write the equations for layer i as

$$\frac{d^{(i)}\mathbf{Y}}{dr} = {}^{(i)}\mathbf{Q}\cdot{}^{(i)}\mathbf{Y} \quad \text{for} \quad r\in[R_{i-1},R_i], \tag{C1}$$

where ${}^{(i)}\mathbf{Y}=(y_1,\ldots,y_{k_i})$ is an abstract vector field with as many entries, say k_i, as there are independent variables in this layer (in most cases, we have four or six independent variables); ${}^{(i)}\mathbf{Q}={}^{(i)}\mathbf{Q}(r,l,\omega)$ is a $k_i\times k_i$ matrix (depending also on the background fields, which we have suppressed in this notation). The variables y_i are placeholders for the corresponding perturbations variables, like H_1, K, V, etc.

Let us now find the general solution in layer i. Since we, a priori, do not have any boundary conditions for this layer, we choose some set of values for ${}^{(i)}\mathbf{Y}(R_{i-1})$ and integrate through this layer using Equation (C1) until we reach $r=R_i$. In order to find the general solution, we repeat this procedure k_i times; each time starting with a different set of values for ${}^{(i)}\mathbf{Y}(R_{i-1})$, where all these 'start vectors' ought to be linearly independent. This generates k_i linearly independent solutions, ${}^{(i)}\mathbf{Y}_j(r)$ (with $j=1,\ldots,k_i$), and the general solution is a linear combination of these, i.e.

$${}^{(i)}\mathbf{Y}(r)=\sum_{j=1}^{k_i}c_{i,j}\,{}^{(i)}\mathbf{Y}_j(r) \quad \text{for} \quad r\in[R_{i-1},R_i], \tag{C2}$$

where the coefficients $c_{i,j}$ with $i = 1, \ldots, n$ (denoting the layer) and $j = 1, \ldots, k_i$ (counting the different solutions inside a particular layer) are constants to be determined by interface and boundary conditions. Before we turn to these, we mention some peculiarities while integrating the different layers. Firstly, in some cases it is possible to reduce the computational effort. This happens if some interface condition essentially is a fixed boundary condition for this layer; for instance, a condition could require a variable to vanish at an interface and we will then, of course, apply this condition when choosing the 'start vectors', effectively reducing the number of linearly independent solutions. Secondly, the innermost layer (number 1 in our way of counting) needs special treatment as the differential equations, due to the use of spherical coordinates, are most likely singular at the origin, $r = 0$. We will therefore expand the solutions at the origin into Taylor series, calculate the Taylor coefficients up to second order and use this expansion up to a small radius at which the ODEs can safely be integrated numerically. Thirdly, the outermost layer n is traditionally integrated from the surface of the star inwards since in most of the cases the Lagrangian pressure perturbation, X, is used as a variable which has to vanish at the surface, $X(R) = 0$.

Finally, we use the (remaining) interface conditions in order to determine the $\sum_i k_i$ coefficients $c_{i,j}$. An interface condition connects the solutions between layer $i-1$ and i. After fixing the overall normalisation by choosing the value of one of the coefficients $c_{i,j}$, we expect to have $(\sum_i k_i) - 1$ interface and boundary conditions (less the conditions we used to reduce the computational effort) in order to uniquely determine the solution. The actual interface conditions can take a variety of forms and a general discussion would go well beyond the scope and necessity; therefore, we restrict ourselves to give two common examples only. First, some variables like the metric perturbations are usually continuous across interfaces, i.e. $[H_1]_{R_i} = 0$, whereas other variables simply vanish, i.e. $T_2(R_i^-) = 0$. The superscript '$-$' in R_i^- is to denote that we consider the limit of T_2 at the inner edge of the interface at radius R_i. These exemplary interface conditions read, respectively

$$[H_1]_{R_i} = 0 \qquad \Leftrightarrow \qquad \sum_{j=1}^{k_i} {c_{i,j}}^{(i)} H_1(R_i) = \sum_{j=1}^{k_{i+1}} {c_{i+1,j}}^{(i+1)} H_1(R_i), \tag{C3}$$

$$T_2(R_i^-) = 0 \qquad \Leftrightarrow \qquad \sum_{j=1}^{k_i} {c_{i,j}}^{(i)} T_2(R_i) = 0. \tag{C4}$$

1. The Boundary Conditions

The problem we are solving involves matching the solution across different interfaces. The simplest case involves the switch from the equations for low frequencies to the formulation of Detweiler & Lindblom [3]. Obviously, all the variables (H_0, H_1, K, V, W and X) have to be continuous at the matching point. Since only four of them are independent, we may freely choose four out of these six. It turns out (by inspection) that it is numerically advantageous to use the set of H_0, K, V and X for matching inside the core ($[H_0]_{R_V} = [K]_{R_V} = [V]_{R_V} = [X]_{R_V} = 0$ in short notation). By choosing those four variables, we find that the condition number of the resulting matrix is some orders of magnitude lower than for other combinations. There are also a couple of other sets for which the matrix has a lower condition number but we are unable to reason this behaviour nor are we able to find a pattern. As a rule of thumb, the variables H_0 and K should be amongst the four chosen ones.

The actual physical interfaces are those which confine the elastic crust. As explained in Section II E, we have five continuous variables at both sides of the elastic crust, namely H_0, H_1, K, W and T_2. We have to use all of them; however, at the core-crust interface, we use the continuity of T_2, and put it in the form $T_2 = 0$ in order to reduce the number of independent solutions in the crust by one, down to five. Formally, we use $[H_0]_{R_{cc}} = [H_1]_{R_{cc}} = [K]_{R_{cc}} = [W]_{R_{cc}} = [H_0]_{R_{co}} = [H_1]_{R_{co}} = [K]_{R_{co}} = [W]_{R_{co}} = 0$ and $T_2(R_{co}^-) = 0$, where R_{cc} and R_{co} are the radii of the core-crust and the crust-ocean interfaces, respectively.

At the center of the star and at the surface, we impose the boundary conditions from Detweiler & Lindblom [3].

[1] K. S. Thorne and A. Campolattaro, *ApJ* **149**, 591 (1967).
[2] L. Lindblom and S. L. Detweiler, *ApJS* **53**, 73 (1983).
[3] S. Detweiler and L. Lindblom, *ApJ* **292**, 12 (1985).
[4] K. D. Kokkotas and B. F. Schutz, *MNRAS* **255**, 119 (1992).
[5] L. S. Finn, *MNRAS* **222**, 393 (1986).
[6] L. S. Finn, *MNRAS* **227**, 265 (1987).
[7] T. E. Strohmayer, *ApJ* **417**, 273 (1993).

[8] G. Miniutti, J. A. Pons, E. Berti, L. Gualtieri, and V. Ferrari, *MNRAS* **338**, 389 (2003).
[9] B. L. Schumaker and K. S. Thorne, *MNRAS* **203**, 457 (1983).
[10] G. L. Comer, D. Langlois, and L. M. Lin, *Phys. Rev. D* **60**, 104025 (1999).
[11] N. Andersson, G. L. Comer, and D. Langlois, *Phys. Rev. D* **66**, 104002 (2002).
[12] L.-M. Lin, N. Andersson, and G. L. Comer, *Phys. Rev. D* **78**, 083008 (2008).
[13] H. Sotani, K. D. Kokkotas, and N. Stergioulas, *MNRAS* **385**, L5 (2008).
[14] A. Colaiuda, H. Beyer, and K. D. Kokkotas, *MNRAS* **396**, 1441 (2009).
[15] M. Gabler, P. Cerdá-Durán, N. Stergioulas, J. A. Font, and E. Müller, *MNRAS* **421**, 2054 (2012).
[16] M. Gabler, P. Cerdá-Durán, N. Stergioulas, J. A. Font, and E. Müller, Physical Review Letters **111**, 211102 (2013), 1304.3566.
[17] V. Ferrari, G. Miniutti, and J. A. Pons, Classical and Quantum Gravity **20**, 841 (2003).
[18] N. Andersson, *ApJ* **502**, 708 (1998).
[19] N. Andersson and K. D. Kokkotas, International Journal of Modern Physics D **10**, 381 (2001).
[20] K. H. Lockitch, N. Andersson, and J. L. Friedman, *Phys. Rev. D* **63**, 024019 (2001).
[21] B. Haskell, N. Andersson, and A. Passamonti, *MNRAS* **397**, 1464 (2009).
[22] A. L. Watts and T. E. Strohmayer, *ApJ* **637**, L117 (2006).
[23] L. Samuelsson and N. Andersson, *MNRAS* **374**, 256 (2007).
[24] A. Colaiuda and K. D. Kokkotas, *MNRAS* **414**, 3014 (2011), 1012.3103.
[25] T. Strohmayer and S. Mahmoodifar, ArXiv e-prints (2013), 1310.5147.
[26] N. Andersson, D. I. Jones, and W. C. G. Ho (2014), in prep.
[27] N. Andersson, K. D. Kokkotas, and N. Stergioulas, *ApJ* **516**, 307 (1999).
[28] R. Bondarescu, S. A. Teukolsky, and I. Wasserman, *Phys. Rev. D* **76**, 064019 (2007).
[29] B. Abbott, R. Abbott, R. Adhikari, J. Agresti, P. Ajith, B. Allen, R. Amin, S. B. Anderson, W. G. Anderson, M. Arain, et al., *Phys. Rev. D* **76**, 062003 (2007), astro-ph/0703419.
[30] J. Abadie, B. P. Abbott, R. Abbott, M. Abernathy, C. Adams, R. Adhikari, P. Ajith, B. Allen, G. Allen, E. Amador Ceron, et al., *ApJ* **722**, 1504 (2010).
[31] J. Abadie, B. P. Abbott, R. Abbott, R. Adhikari, P. Ajith, B. Allen, G. Allen, E. Amador Ceron, R. S. Amin, S. B. Anderson, et al., *Phys. Rev. D* **83**, 042001 (2011).
[32] J. Abadie, B. P. Abbott, R. Abbott, M. Abernathy, T. Accadia, F. Acernese, C. Adams, R. Adhikari, C. Affeldt, B. Allen, et al., *ApJ* **734**, L35 (2011).
[33] P. S. Shternin, D. G. Yakovlev, C. O. Heinke, W. C. G. Ho, and D. J. Patnaude, *MNRAS* **412**, L108 (2011).
[34] N. Chamel, *MNRAS* **388**, 737 (2008).
[35] N. Andersson, C. Krüger, G. L. Comer, and L. Samuelsson, Classical and Quantum Gravity **30**, 235025 (2013).
[36] K. Glampedakis, N. Andersson, and L. Samuelsson, *MNRAS* **410**, 805 (2011).
[37] C. W. Misner, K. S. Thorne, and J. A. Wheeler, *Gravitation* (1973).
[38] N. Andersson and K. D. Kokkotas, *MNRAS* **299**, 1059 (1998).
[39] P. B. Demorest, T. Pennucci, S. M. Ransom, M. S. E. Roberts, and J. W. T. Hessels, *Nature* **467**, 1081 (2010).
[40] J. Antoniadis, P. C. C. Freire, N. Wex, T. M. Tauris, R. S. Lynch, M. H. van Kerkwijk, M. Kramer, C. Bassa, V. S. Dhillon, T. Driebe, et al., Science **340**, 448 (2013).
[41] A. W. Steiner, J. M. Lattimer, and E. F. Brown, *ApJ* **722**, 33 (2010).
[42] P. Haensel and A. Y. Potekhin, *A&A* **428**, 191 (2004).
[43] W. C. G. Ho, K. Glampedakis, and N. Andersson, *MNRAS* **422**, 2632 (2012), [erratum: **425**, 1600 (2012)].
[44] G. F. Burgio, V. Ferrari, L. Gualtieri, and H.-J. Schulze, *Phys. Rev. D* **84**, 044017 (2011).
[45] F. Douchin and P. Haensel, *A&A* **380**, 151 (2001).
[46] K. A. van Riper, *ApJS* **75**, 449 (1991).
[47] D. G. Yakovlev, K. P. Levenfish, and Y. A. Shibanov, Physics Uspekhi **42**, 737 (1999).
[48] D. Page, J. M. Lattimer, M. Prakash, and A. W. Steiner, *ApJS* **155**, 623 (2004).
[49] D. G. Yakovlev, A. D. Kaminker, and K. P. Levenfish, *A&A* **343**, 650 (1999).
[50] D. G. Yakovlev, A. D. Kaminker, O. Y. Gnedin, and P. Haensel, *Phys. Rep.* **354**, 1 (2001).
[51] E. Flowers and N. Itoh, *ApJ* **230**, 847 (1979).
[52] E. Flowers and N. Itoh, *ApJ* **250**, 750 (1981).
[53] D. A. Baiko, P. Haensel, and D. G. Yakovlev, *A&A* **374**, 151 (2001).
[54] P. S. Shternin and D. G. Yakovlev, *Phys. Rev. D* **75**, 103004 (2007).
[55] URL `http://www.ioffe.ru/astro/conduct/`.
[56] A. Y. Potekhin, D. A. Baiko, P. Haensel, and D. G. Yakovlev, *A&A* **346**, 345 (1999).
[57] S. Cassisi, A. Y. Potekhin, A. Pietrinferni, M. Catelan, and M. Salaris, *ApJ* **661**, 1094 (2007).
[58] A. I. Chugunov and P. Haensel, *MNRAS* **381**, 1143 (2007).
[59] E. H. Gudmundsson, C. J. Pethick, and R. I. Epstein, *ApJ* **259**, L19 (1982).
[60] A. Y. Potekhin, D. G. Yakovlev, G. Chabrier, and O. Y. Gnedin, *ApJ* **594**, 404 (2003).
[61] R. T. Farouki and S. Hamaguchi, Phys. Rev. E **47**, 4330 (1993).
[62] A. Reisenegger and P. Goldreich, *ApJ* **395**, 240 (1992).
[63] S. L. Detweiler and J. R. Ipser, *ApJ* **185**, 685 (1973).
[64] M. Prakash, I. Bombaci, M. Prakash, P. J. Ellis, J. M. Lattimer, and R. Knorren, *Phys. Rep.* **280**, 1 (1997).
[65] A. J. Penner, N. Andersson, L. Samuelsson, I. Hawke, and D. I. Jones, *Phys. Rev. D* **84**, 103006 (2011).

[66] T. Regge and J. A. Wheeler, Physical Review **108**, 1063 (1957).
[67] L. S. Finn, *MNRAS* **245**, 82 (1990).
[68] H. Sundqvist and G. Veronis, Tellus **22**, 26 (1970).
[69] N. Andersson, K. D. Kokkotas, and B. F. Schutz, *MNRAS* **274**, 1039 (1995).
[70] T. G. Cowling, *MNRAS* **101**, 367 (1941).
[71] P. N. McDermott, H. M. van Horn, and C. J. Hansen, *ApJ* **325**, 725 (1988).
[72] Note that the problem changes if we want to account for superfluid components.